Development and Performance Evaluation of a WT-LSTM Hybrid Model for Global Land Meteorological Drought Prediction

Jinfeng Bu[1,2★], Kebiao Mao[1,3,4★], Xueqi Xia[2], Jiancheng Shi[6], Sayed M. Bateni[5], Zijin Yuan[1]

1. State Key Laboratory of Efficient Utilization of Arid and Semi-arid Arable Land in Northern China, Institute of agricultural resources and regional planning, Chinese Academy of Agricultural Sciences, Beijing, 100081, China. yuanzijin@caas.cn

2. School of Earth Sciences and Resources, China University of Geosciences, Beijing, 100083, China. xiaxueqi@cugb.edu.cn

3.School of Physics and Electronic-Engineering, Ningxia University, Yinchuan 750021, China.

4. School of Surveying and Geo-Informatics, Shandong Jianzhu University, Jinan, 250100, China.

5.Department of Civil and Environmental Engineering and Water Resources Research Center, University of Hawaii at Manoa, Honolulu, HI 96822, USA; smbateni@hawaii.edu

6.National Space Science Center, Chinese Academy of Sciences, Beijing, 100190, China. shijiancheng@nssc.ac.cn

Correspondence to: Kebiao Mao (maokebiao@caas.cn)

Tel.: +86-010-8210-8769

Declarations:

Conflict of Interest: The authors declared that they have no conflict of interest.

Funding: Central Public-interest Scientific Institution Basal Research Fund (No. Y2025YC86) and the Key Project of Natural Science Foundation of Ningxia Department of Science and Technology (No. 2024AC02032).

Acknowledgments: The authors are grateful to three reviewers and the editor for their constructive comments and suggestions on this paper. The authors extend their heartfelt appreciation to ECMWF for providing the climate reanalysis product and TensorFlow for offering the sophisticated machine learning library that served as the cornerstone for conducting these experiments.

Citation: J.F. Bu, K.B. Mao, X.Q. Xia, J.C Shi, S. M. Bateni, Z. Yuan, Development and Performance Evaluation of a WT-LSTM Hybrid Model for Global Land Meteorological Drought Prediction, EarthArXiv, 2025, 6, DOI: .

Subjects：Engineering, Physical Sciences and Mathematics

Keywords：Artificial Intelligence, Drought, WT-LSTM Hybrid Model, Prediction

Dates Published:

Development and Performance Evaluation of a WT-LSTM Hybrid Model for Global Land Meteorological Drought Prediction

Jinfeng Bu[1,2★], Kebiao Mao[1,3,4★], Xueqi Xia[2], Jiancheng Shi[6], Sayed M. Bateni[5], Zijin Yuan[1]

1. State Key Laboratory of Efficient Utilization of Arid and Semi-arid Arable Land in Northern China, Institute of agricultural resources and regional planning, Chinese Academy of Agricultural Sciences, Beijing, 100081, China. yuanzijin@caas.cn

2. School of Earth Sciences and Resources, China University of Geosciences, Beijing, 100083, China. xiaxueqi@cugb.edu.cn

3.School of Physics and Electronic-Engineering, Ningxia University, Yinchuan 750021, China.

4. School of Surveying and Geo-Informatics, Shandong Jianzhu University, Jinan, 250100, China.

5.Department of Civil and Environmental Engineering and Water Resources Research Center, University of Hawaii at Manoa, Honolulu, HI 96822, USA; smbateni@hawaii.edu

6.National Space Science Center, Chinese Academy of Sciences, Beijing, 100190, China. shijiancheng@nssc.ac.cn

Correspondence to: Kebiao Mao (maokebiao@caas.cn)

★ These authors contributed equally to this work.

Key Points:

- A hybrid model that combines wavelet transform and long short-term memory neural network (WT-LSTM) has been constructed.
- Based on historical SPEI drought index data, the hybrid model is used to predict drought variations.
- By integrating multiple factors such as precipitation, land surface temperature, and potential evapotranspiration, the hybrid model predicts drought variations.
- The hybrid model outperforms traditional time series prediction models in capturing spatiotemporal information.

Abstract. In recent years, droughts have become increasingly frequent worldwide, leading to issues such as reduced agricultural yields and ecological degradation in various regions. To mitigate the impact of drought on human survival and development, this study utilizes the Standardized Precipitation Evapotranspiration Index (SPEI) to analyze the spatiotemporal variations of global droughts. The results reveal a clear trend of increasing drought in regions such as Africa, South America, and Asia. To improve the accuracy of global drought prediction, a hybrid model combining wavelet transform and long short-term memory neural networks (WT-LSTM) was developed. Based on this hybrid model, two forecasting schemes were designed: the first scheme leverages deep learning on historical SPEI data to predict drought trends, while the second scheme integrates multiple factors, including precipitation, land surface temperature, and potential evapotranspiration, to forecast drought variations. Analysis using multi-source data from 1979 to 2022 shows that the WT-LSTM model outperforms traditional time series models in capturing spatiotemporal patterns. Both schemes demonstrated strong performance in model training and testing, achieving high prediction accuracy with a one-month lead time (Scheme 1: mean absolute error < 0.50, Pearson correlation > 0.80; Scheme 2: mean absolute error < 0.35, Pearson correlation > 0.90). The comparison between the two schemes indicates a high spatial consistency, with Scheme 2 exhibiting a clear advantage in drought prediction. The model was further applied to identify and reconstruct drought characteristics from 2013 to 2022 in typical drought-prone regions, revealing that Scheme 2 significantly outperforms Scheme 1 in reproducing drought duration and intensity. This indicates strong capability in drought feature recognition and regional adaptability. Overall, the proposed method provides effective technical support for meteorological drought forecasting, helping policymakers and the public to take early emergency measures, reduce agricultural losses, and raise awareness of drought issues. Especially in the context of escalating climate change, interdisciplinary collaboration and research are crucial for developing comprehensive and effective strategies to address global sustainable development challenges.

Plain Language Summary: In recent years, droughts have been happening more often around the world, causing problems like lower crop yields and harm to the environment. This study looks at how drought patterns have changed globally using the Standardized Precipitation Evapotranspiration Index (SPEI). The findings show that droughts are increasing in places like Africa, South America, and Asia. To predict these droughts better, we created a hybrid model that combines wavelet transform and long short-term memory neural network (WT-LSTM). We designed two methods for predicting drought: one using past SPEI data and another that includes factors like rainfall and temperature. The results show that the hybrid model is more accurate than traditional methods. Both prediction methods performed well, with Scheme 2 being especially effective. This research can help improve drought forecasting, leading to quicker responses and less damage to agriculture.

1. Introduction

Meteorological drought, as one of the most common natural disasters globally, poses severe threats to agricultural production, water resource management, and the stability of ecosystems. With the intensification of climate change, the frequency and intensity of drought events are increasing, presenting unprecedented challenges to global food security and sustainable water resource management. Addressing the challenges of meteorological drought requires interdisciplinary collaboration and research, involving fields such as meteorology, agricultural science, ecology, and economics. The impacts of climate change extend beyond the climate system and are closely linked to socioeconomic development, policy formulation, and public awareness. Therefore, accurately understanding and predicting the spatiotemporal variation patterns of global land meteorological drought is not only a crucial aspect of meteorological and hydrological research but also a key prerequisite for achieving the United Nations Sustainable Development Goals.

In the process of monitoring and analyzing drought, selecting appropriate indices to determine the spatiotemporal distribution and trends of drought is essential. Currently, over 160 drought indices have been developed to analyze the spatiotemporal variations of drought, each demonstrating its unique advantages and limitations. The Standardized Precipitation Evapotranspiration Index (SPEI), in particular, considers both precipitation and potential evapotranspiration, providing a more comprehensive reflection of a region's hydrological and climatic conditions rather than relying on a single climatic factor. Studies have shown that SPEI is more accurate in identifying the severity and duration of drought compared to simpler indices like the Standardized Precipitation Index (SPI)(Tirivarombo et al., 2018). For example, in the Kafue River Basin in northern Zambia, SPEI more effectively captured the drought sequence changes from 1960 to 2015 compared to SPI. Additionally, other indices like SCPDSI, although providing estimates of drought severity, often exhibit discrepancies with actual conditions and show a lag in the evolution of drought. Therefore, SPEI is chosen as the primary index for analyzing global droughts to provide more accurate and comprehensive drought assessments.

Given the complexity of time series data types, developing accurate prediction models often faces significant challenges. Over the years, many prediction models have been established, including regression models (Sun et al., 2012), conditional probability models (Hao et al., 2016), data-driven models (Xu et al., 2020), and machine learning algorithms (Xu et al., 2022). Each method has its strengths and weaknesses. For instance, in data-driven models, the Autoregressive Integrated Moving Average (ARIMA) model performs well in long-term drought prediction, but it struggles to capture nonlinear characteristics (Kim et al., 2022, Wang, 2022). In recent years, machine learning has become a core component of data-driven research in Earth sciences, widely applied in the study of the atmosphere, land surface, and oceans (Ham et al., 2019, Reichstein et al., 2019, Asgarimehr et al., 2022, Liu et al., 2022, Retsch et al., 2022, Zhang et al., 2022, Zheng et al., 2022). Specifically, in meteorology, methods like the Random Forest (RF) model are extensively used to address problems in Earth sciences and remote sensing (Gislason et al., 2006).

In the field of deep learning, Artificial Neural Networks (ANNs) have been widely adopted due to their excellent capability in time series prediction, especially in capturing nonlinear information in data. However, as the number of parameters increases and training time lengthens, there has been a shift towards other nonlinear models such as Recurrent Neural Networks (RNNs), which are suitable for tasks based on short-term memory but are less sensitive to older data (Le et al., 2017). To achieve long-term predictions, the Long Short-Term Memory (LSTM) model, based on RNNs, was developed, characterized by more complex neuron structures (Dikshit et al., 2021). Additionally, wavelet transform, as a data preprocessing tool, has been proven to successfully decompose raw data and effectively predict nonlinear and non-stationary time series (Madhu et al., 2015), significantly enhancing the performance of machine learning models. The Wavelet Transform Long Short-Term Memory (WT-LSTM) model, combining wavelet transform and LSTM, has shown excellent performance in hydrological forecasting, although its application in short-term meteorological drought forecasting is still relatively limited.

In the complex context of addressing meteorological drought, the rapid development of artificial intelligence (AI) technologies presents new opportunities for improving drought prediction accuracy. Meteorological drought not only involves climate change but also relates to multiple fields, including agricultural production, ecological environment, and socio-economics. Therefore, interdisciplinary collaboration is especially important. Deep learning technologies have demonstrated exceptional performance in analyzing large-scale, high-dimensional meteorological data, enabling the identification and extraction of complex patterns and potential information related to drought development. This not only improves prediction accuracy but also provides a scientific basis for decision-makers. This study integrates the characteristics of multiple disciplines by combining meteorological analysis, mathematical modeling, and deep learning methods to deeply analyze the spatiotemporal variations of global drought using the Standardized Precipitation Evapotranspiration Index (SPEI), aiming to provide new insights for global drought monitoring and response. To better predict drought changes, we design a hybrid model that combines wavelet transformation and Long Short-Term Memory (LSTM) neural networks (WT-LSTM). We propose two predictive approaches: the first approach utilizes WT-LSTM to perform deep learning on historical SPEI index data to predict drought trends; the second approach integrates multiple factors, including precipitation, surface temperature, and potential evapotranspiration, to achieve a more comprehensive drought change prediction. This comprehensive research methodology not only enhances the accuracy of predictions but also aids policymakers in effectively responding to the challenges posed by climate change, while raising public awareness and concern regarding drought issues, thus promoting the achievement of global sustainable development goals.

2. Study Area and Data

2.1 Study Area

To comprehensively understand the variations in drought across different geographical regions, the study encompasses the main land-based grain-producing areas globally, spanning Asia, Europe, South America, North America, Oceania, and Africa, covering six continents excluding Antarctica, as shown in Figure 1. To improve computational efficiency and ensure the accuracy of the research results, an effective data processing method was adopted: bilinear interpolation of the raw data to a resolution of $1° \times 1°$. By interpolating the data to a lower spatial resolution, we can significantly reduce the data volume while retaining sufficient geographical information, thereby reducing computational complexity and enhancing computational efficiency. Bilinear interpolation is a commonly used and effective interpolation method that performs linear interpolation on the original data in both horizontal and vertical directions, converting the data to a target resolution grid. This method can reduce the spatial complexity of the data while preserving spatial correlations to a certain extent, making the interpolated data more representative of the actual situation. The spatial analysis and prediction of drought on a global scale reveal key characteristics such as the frequency, intensity, and duration of drought in different regions. This helps us better understand the spatiotemporal distribution patterns of drought events, thereby providing scientific basis for disaster risk assessment and the formulation of response measures in relevant regions. Especially against the backdrop of global challenges such as climate change, resource depletion, and ecological degradation, enhancing our understanding and predictive capacity regarding drought issues is crucial for formulating sustainable development policies.

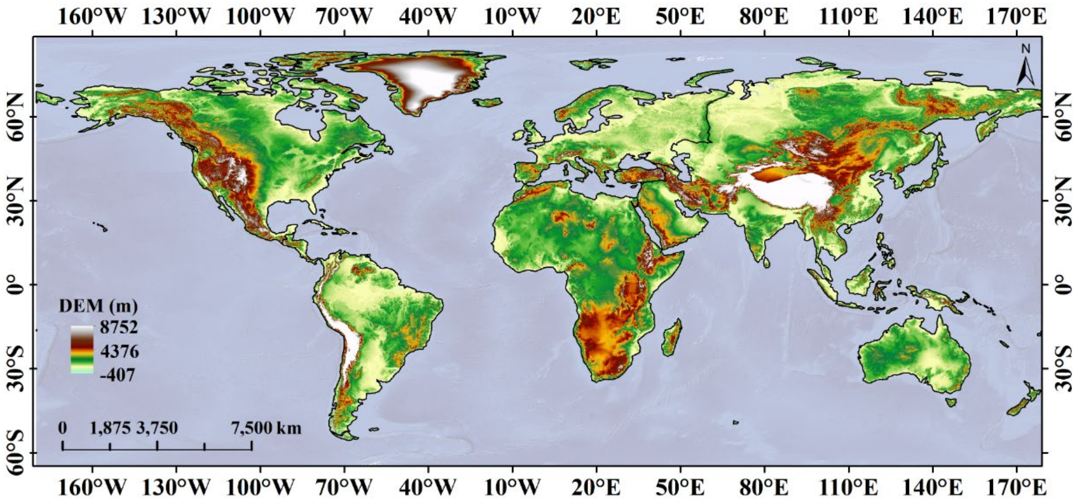

Figure 1. Overview of the Study Area (excluding Antarctica)

2.2 Data

2.2.1 ERA5 Data

The ERA5 dataset includes data on precipitation (Pre), potential evapotranspiration (PET), evaporation (e), Volumetric soil water layer 1 (SWVL1)(0-7cm), land surface temperature (LST), 10m u-component of wind (u10), and 10m v-component of wind (v10) for the selection of predictor variables. The precipitation data uses hourly precipitation amounts with a spatial resolution of 0.25°, which are summed to obtain monthly precipitation amounts. Potential evapotranspiration data is calculated using the FAO-modified Penman-Monteith formula. Although the ERA5 dataset contains information since 1940, some issues have been identified before 1970. For this reason, we focus on the period from 1979 to 2022. ERA5 is the latest reanalysis dataset from the European Centre for Medium-Range Weather Forecasts (ECMWF), replacing ERA-Interim, which has proven reliable for investigating climate change.

2.2.2 CRU and SPEIBase

The latest time series version (CRU TS v. 4.07) is a station-based gridded time series dataset providing monthly estimates of various variables, including precipitation, at a 0.5° resolution for the period from 1901 to 2022. Several studies have shown that CRU data captures many spatiotemporal characteristics of various surface climate variables. To verify the reliability of SPEI in the study, we used the SPEIbase dataset for the period from 1979 to 2022. The SPEI database is based on monthly precipitation and potential evapotranspiration data from the Climatic Research Unit (CRU) of the University of East Anglia, estimated using the FAO-56 Penman-Monteith method. SPEIbase provides SPEI data across multiple time scales from 1 to 48 months, with a spatial resolution of 0.5° and a temporal resolution of one month, covering the period from January 1901 to December 2022. SPEIBase has been evaluated and applied in many studies. In comparative analysis, to match the spatial resolution of SPEI, the spatial resolution of the newly developed SPEIBase was resampled to 1° using a bilinear method.

2.2.3 Ground observation station data

This study utilizes meteorological station data provided by the National Centers for Environmental Information (NCEI) under the National Oceanic and Atmospheric Administration (NOAA) to study the impact of climate change on surface water resources. Precipitation data covers continuous observation records from 1929 to the present, with a frequency of daily or monthly, depending on the observation strategy of each meteorological station (https://www.ncei.noaa.gov/maps/monthly/). Monthly precipitation data from typical regions for the period from 1979 to 2022 were extracted, and the FAO-modified Penman-Monteith formula was used to calculate potential evapotranspiration to validate the accuracy of the predicted SPEI index data.

3. Methodology

Previous studies have mainly focused on time series analysis of regionally averaged variables, with relatively few investigations into the joint spatiotemporal evolution of droughts (Mishra and Singh, 2011). Moreover, while most existing research has concentrated on drought prediction at longer time scales, analyses and forecasts at shorter time scales have not received sufficient attention. Therefore, the focus of this study begins with the selection of predictor variables, analyzing and visualizing the spatiotemporal trends of predictors and drought, along with significance testing to examine potential drought development trends. Next, drought events are effectively identified by visualizing and quantifying drought duration, extent, and severity from 1979 to 2022. Finally, data transformation is conducted, extracting features from multi-source data, applying normalization as needed, performing sliding window operations, and using DMeyer wavelet decomposition to smooth the data. This enhances the richness and diversity of the dataset to ensure model stability and convergence. Two schemes are used to integrate this process with an LSTM model for prediction. The data are divided into a training set (1979–2012) and a validation set (2013–2022), with predictive accuracy compared against a standalone LSTM model. Site-specific validation and cross-validation are conducted to assess forecasting performance, followed by identification and reconstruction analysis of drought characteristics in typical drought-prone regions from 2013 to 2022(Figure 2).

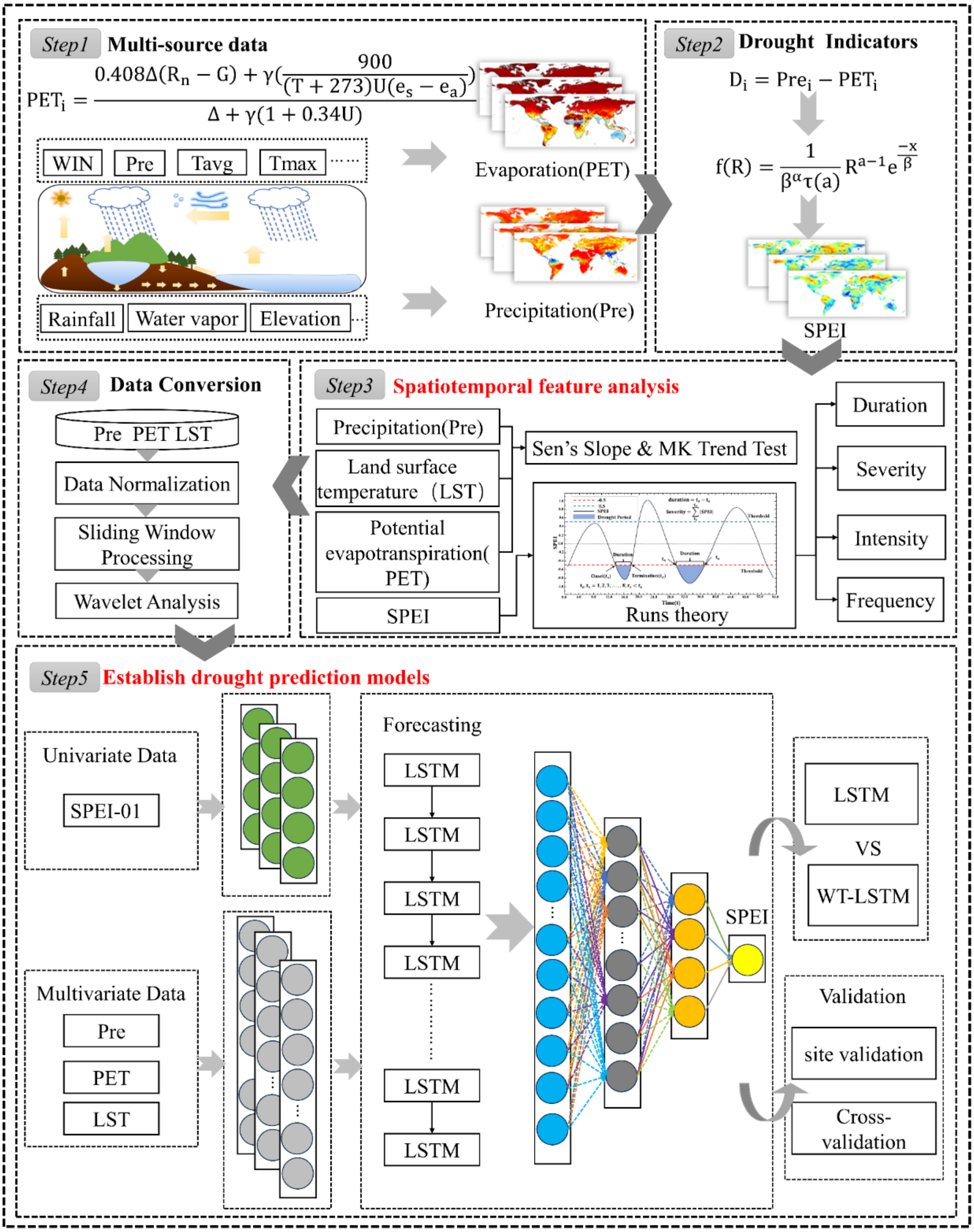

Figure 2. Framework for the Analysis and Prediction of Spatiotemporal Characteristics of Meteorological Drought

3.1 Drought Index and Drought Event Identification

3.1.1 Drought Index

The Standardized Precipitation Evapotranspiration Index (SPEI) is an improved drought index that considers both atmospheric precipitation and potential evapotranspiration factors, making it suitable for studying the impact of global warming on drought severity. It is based on the probability distribution of the difference between accumulated precipitation and potential evapotranspiration over different time scales. The multi-scale nature of

SPEI allows for the identification of various types of drought and their impacts (Vicente-Serrano et al., 2010). SPEI enables users to assess the occurrence of short-term (duration of 1 month), medium-term (3 to 12 months), and long-term droughts (12 months and longer) (Guttman, 1999, Łabędzki, 2007, Trnka et al., 2008).

The calculation of SPEI depends on the cumulative deficit or surplus (D_i)of the water balance over different time scales. D_i can be determined based on the precipitation (Pre) and potential evapotranspiration (PET) on a given date by equation (1).

$$D_i = \mathrm{Pre} - \mathrm{PET} \qquad (1)$$

To obtain the SPEI series, the water balance needs to be normalized to a probability distribution. The optimal distribution for SPEI calculation is the Generalized Extreme Value (GEV) distribution (Stagge et al., 2015, Wang et al., 2021), which can overcome the limitations of the original SPEI with the Generalized Logistic distribution for short-term accumulations (1 to 2 months) (Vicente-Serrano et al., 2010). Therefore, we use the GEV distribution to standardize the D series into the SPEI data series (Wang et al., 2021).

The probability distribution function of the D series is given by the following equation (2).

$$F(x) = \left[1 + \left(\frac{\alpha}{x-\gamma}\right)^{\beta}\right]^{-1} \qquad (2)$$

In the formula, α, β, and γ represent the scale, shape, and location parameters, respectively.

3.1.2 Theil-Sen Median Slope Estimation and Mann-Kendall Test

The Theil-Sen Median method, also known as Sen's slope estimation, is widely used in temporal dynamic analysis to explore interannual variation characteristics (Peng et al., 2016). The Theil-Sen median trend analysis is a non-parametric statistical method (Sen, 1968, Theil, 1950)suitable for analyzing long-term series trends. The calculation formula is equation (3).

$$\beta = \mathrm{mean}\left(\frac{x_j - x_i}{j-1}\right), \forall j > i \qquad (3)$$

Where x_j and x_i are the time series data. If β is greater than 0, the time series shows an upward trend; if β is less than 0, the time series shows a downward trend.

The non-parametric Mann-Kendall (MK) test (Mann, 1945) is commonly used to assess the significance of monotonic trends in time series data related to climate, meteorology, and hydrology (Cailas et al., 1986, Hipel et al., 1988, Zetterqvist, 1991, Chiew et al., 1993, Yue et al., 2002, Onoz et al., 2003, Yue et al., 2004, Topaloğlu et al., 2012, Yu et al., 1993, Gan, 1998, Lins et al., 1999, Douglas et al., 2000). The MK test statistic (S) is calculated using the following equation (4-5).

$$\mathrm{sgn}(x_j - x_i) = \begin{cases} 1; & \text{If } x_j > x_i \\ 0; & \text{If } x_j = x_i \\ -1; & \text{If } x_j < x_i \end{cases} \qquad (4)$$

$$S = \sum_{i=1}^{n-1} \sum_{j=i+1}^{n} \mathrm{sgn}(x_j - x_i) \qquad (5)$$

Where x_i and x_j are the represent time series data for precipitation, land surface temperature, potential evapotranspiration, and the SPEI index at times i and j, respectively, and n represents the length of the data set. A positive S indicates an upward trend, while a negative S indicates a downward trend. The following expressions are used as hypotheses for a data series with length $n > 10$ and an approximately normal distribution (variance ($\sigma 2 = 1$) and mean ($\mu = 0$)).

$$\mathrm{Var}(S) = \frac{n(n-1)(2n+5) - \sum_{i=1}^{P} t_i(t_i-1)(2t_i+5)}{18} \qquad (6)$$

In this equation(6), P represents the number of tied groups, and the summation symbol ($\sum$) denotes the total sum across all tied groups. t_i indicates the number of data values in the i-th tied group. If there are no tied groups, this summarization process can be disregarded. After calculating the variance of the time series data using equation (11), the standard Z-score can be computed according to equation (7).

$$Z = \begin{cases} \frac{S-1}{\sqrt{Var(S)}}; & \text{If } S > 0 \\ 0; & \text{If } S = 0 \\ \frac{S+1}{\sqrt{Var(S)}}; & \text{If } S < 0 \end{cases} \quad (7)$$

The calculated standard Z-value is compared with the critical values from the standard normal distribution table for two-tailed confidence levels ($\alpha = 10\%, \alpha = 5\%, \text{and } \alpha = 1\%$). If $|Z| > |Z1 - \alpha/2|$, the null hypothesis (H0) is rejected, indicating that the trend is statistically significant. Otherwise, the null hypothesis (H0) is accepted, meaning that the trend is not statistically significant and there is no trend in the time series (no trend time series). In this study, the MK method uses a 95% two-tailed confidence level.

3.1.3 Identification of Drought Events

Run theory is a method for extracting drought events based on the characteristics of the drought index in a time series by setting relevant thresholds (Yevjevich, 1967). The specific process for identifying drought events using the threshold method is as follows: set the threshold to -0.5 (Wu et al., 2019). Values below the threshold indicate the start of a drought event, while values returning to or exceeding the threshold indicate the end of the drought event. Drought duration is defined as the length of time the value remains below the threshold by equation (8). Drought severity refers to the total absolute value of SPEI during the drought event by equation (9), and drought intensity is calculated by dividing drought severity by drought duration by equation (10), as shown in Figure 3.

$$\text{Drought duration} = t_e - t_s \quad (8)$$

$$\text{Drought severity} = \sum_{t_s}^{t_e} |\text{SPEI}| \quad (9)$$

$$\text{Drought intensity} = \frac{\text{Drought severity}}{\text{Drought duration}} \quad (10)$$

Here, t_e and t_s represent the end and start times of the drought event, respectively, and SPEI represents the drought index.

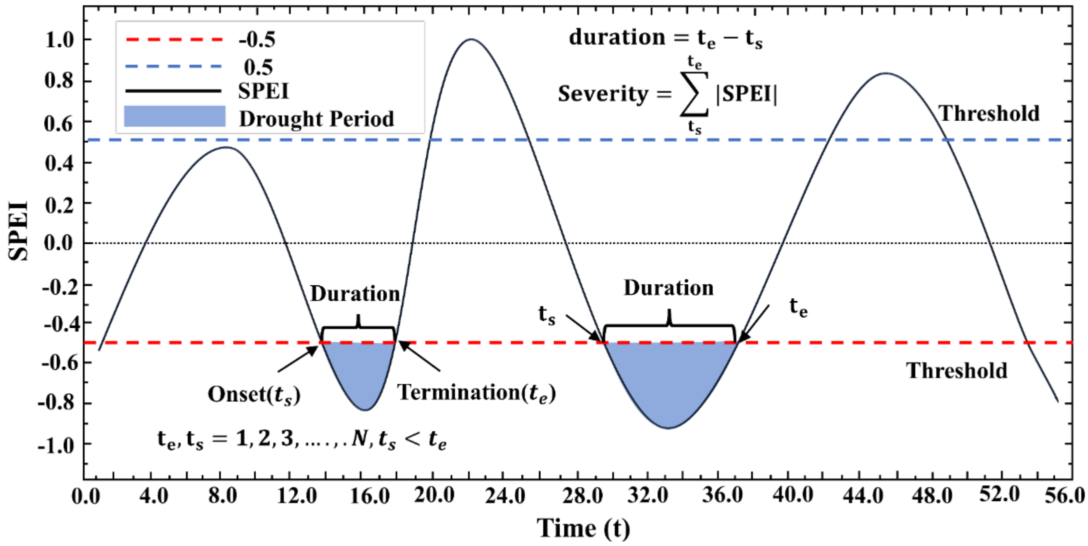

Figure 3. Schematic Diagram of Run Theory Run Theory Diagram (Extracting Drought Duration, Severity, Intensity, and Frequency from SPEI Time Series, where the time series is denoted as t=1, 2, ..., N)

3.2 Discrete Wavelet

Wavelet analysis can be divided into Continuous Wavelet Transform (CWT) and Discrete Wavelet Transform (DWT). Continuous Wavelet Transform is not commonly used for prediction due to its computational difficulty and processing time requirements (Kisi, 2011). Discrete Wavelet Transform, on the other hand, is often used for prediction because of its lower computational load and simpler application. DWT is given by equation (11).

$$\psi_{m,n}(\mathrm{t}) = \frac{1}{\sqrt{s_o^m}}\psi\left\{\frac{t-n\tau_o s_o^m}{s_o^m}\right\} \tag{11}$$

Where m and n are integers that control scale and time, respectively; m(t) is the mother wavelet. The most common choices for the parameters S_o and τ_o are 2 and 1, respectively. According to Mallat's theory, a discrete time series can be decomposed into a series of linear neutral approximation signals and detail signals through the inverse discrete wavelet transform. Equation (12) gives the inverse DWT according to Mallat (1989)(Mallat, 1989).

$$\mathrm{x(t)} = \mathrm{T} + \sum_{\mathrm{m=1}}^{\mathrm{M}}\sum_{\mathrm{t=0}}^{2^{\mathrm{M-m-1}}} \mathrm{W_{m,n}} 2^{-\frac{\mathrm{m}}{2}}\psi(2^{-\mathrm{m}}\mathrm{t} - \mathrm{n}) \tag{12}$$

Where $W_{m,n} = 2^{-\frac{m}{2}}\sum_{t=0}^{N-1}\psi(2^{-m}t - n)x(t)$ is the wavelet coefficient of the discrete wavelet at scale $\mathrm{s} = 2^{\mathrm{m}}$ and $\tau = 2^m n$. This method includes two stages: decomposition and reconstruction. First, the Dmeyer mother wavelet is selected, with a decomposition level of 3. The sequence is decomposed into high-pass (detail) and low-pass (approximation) filters, extracting the high-frequency and low-frequency components of the sequence, respectively. The low-frequency signal (approximation) is estimated using a prediction model, while the detail signal (noise) is trained separately using a neural network. A new signal is reconstructed from the predicted values of the approximation and detail sub-series using the inverse wavelet transform. Finally, the combined prediction is obtained by summing the predictions of these two components.

3.3 LSTM Model

The Long Short-Term Memory network (LSTM), a special type of Recurrent Neural Network (RNN) model, exhibits excellent performance in time series data modeling. Compared to traditional RNNs, LSTMs are unique due to the complex structure of their hidden layers and the introduction of the cell state structure. This structure controls the flow of memory information, allowing for long-term transmission and memory of information (Yang et al., 2019). Due to these characteristics, LSTM models are widely used for sequence data where long-term information needs to be considered, and they can handle longer time steps (Cui et al., 2022), as shown in Figure 4.

Given $\mathrm{x_t}$ as the input at the current time step and $\mathrm{h_{t-1}}$ as the hidden state from the previous time step. Assuming the number of hidden units is l, the mini-batch input at a given time step is $\mathrm{x_t} \in \mathrm{R}^{\mathrm{n\times m}}$ (where n is the number of samples and m is the number of inputs), and $\mathrm{h_{t-1}} \in \mathrm{R}^{\mathrm{n\times l}}$. The input gate $\mathrm{i_t} \in \mathrm{R}^{\mathrm{n\times m}}$, forget gate $\mathrm{f_t} \in \mathrm{R}^{\mathrm{n\times m}}$, output gate $\mathrm{o_t} \in \mathrm{R}^{\mathrm{n\times m}}$, and hidden state $\mathrm{h_t} \in \mathrm{R}^{\mathrm{n\times m}}$ at the time step are calculated by equation (13-17).

$$\mathrm{i_t} = \sigma(\mathrm{W_{xi}x_t} + \mathrm{W_{hi}h_{t-1}} + \mathrm{b_i}) \tag{13}$$

$$\mathrm{f_t} = \sigma(\mathrm{W_{xf}x_t} + \mathrm{W_{hf}h_{t-1}} + \mathrm{b_f}) \tag{14}$$

$$\mathrm{c_t} = \tanh(\mathrm{W_{xc}x_t} + \mathrm{W_{hc}h_{t-1}} + \mathrm{b_c}) \tag{15}$$

$$\mathrm{o_t} = \sigma(\mathrm{W_{xo}x_t} + \mathrm{W_{ho}h_{t-1}} + \mathrm{b_o}) \tag{16}$$

$$\mathrm{h_t} = \mathrm{o_t}\tanh(\mathrm{c_t}) \tag{17}$$

In the formula, $\mathrm{W_{xi}, W_{xf}, W_{xo}, W_{xc}} \in \mathrm{R}^{\mathrm{d\times m}}, \mathrm{W_{hi}, W_{hf}, W_{ho}, W_{hc}} \in \mathrm{R}^{\mathrm{m\times m}}$ are weight parameters, and $\mathrm{b_i, b_f, b_c, b_o} \in \mathrm{R}^{1\times \mathrm{m}}$ are bias parameters. σ denotes the sigmoid activation function.

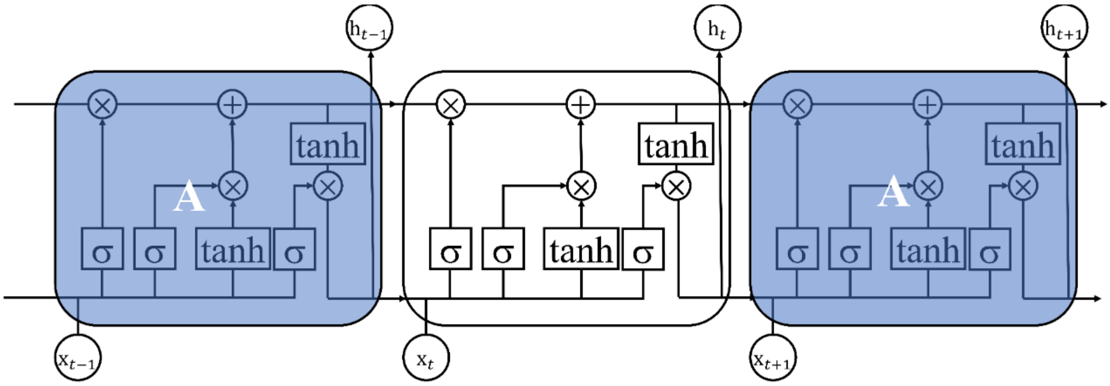

Figure 4. Diagram of the LSTM Model ($x_t$and h_t represent the input and output states at time t; σ and tanh are the sigmoid and hyperbolic tangent activation functions; ⊕ and ⊗ represent addition and multiplication)

To evaluate the performance of each prediction model, we used the following evaluation metrics: Mean Absolute Error (MAE), Mean Squared Error (MSE), Root Mean Squared Error (RMSE), the ratio of RMSE to the standard deviation of observed values (RSR), the Ratio of Standard Deviation (RSD), Nash-Sutcliffe Efficiency Coefficient (NSE), and Correlation Coefficient (R). These metrics are used to assess the performance of hybrid models compared to traditional models, the spatial distribution prediction accuracy of the model at a one-time lead, and the extent to which the model explains the variability in the observed data. We use these evaluation metrics to comprehensively assess the performance of each model on the test set and visually compare their performance through charts.

4. Results and Discussion

4.1 Selection of Predictive Factors

The selection of predictive variables is crucial for developing machine learning and deep learning models. The Pearson correlation coefficient is used to identify the set of important predictive variables, with the results shown in Figure 5. Meteorological drought is a complex process that can be influenced by many factors. Seven meteorological variables are considered as potential influencing factors for the SPEI index: precipitation (Pre), potential evapotranspiration (PET), land surface temperature (LST), 10m U wind component (u10), 10m V wind component (v10), evaporation (e), and volumetric soil water layer 1 (swvl1). The results indicate that precipitation, land surface temperature, and potential evapotranspiration are the main factors affecting SPEI. Drought usually results from a prolonged accumulation of insufficient precipitation. Precipitation provides input, and it is positively correlated with SPEI; drought decreases as precipitation increases, with an average correlation coefficient of 0.51. The trend for temperature is opposite; temperature influences soil moisture loss through its effect on potential evapotranspiration and heat flux, thereby affecting drought. Potential evapotranspiration is negatively correlated with the SPEI index, with drought increasing as potential evapotranspiration increases. Therefore, we selected potential evapotranspiration, land surface temperature, and precipitation as predictive factors for drought prediction using the SPEI index.

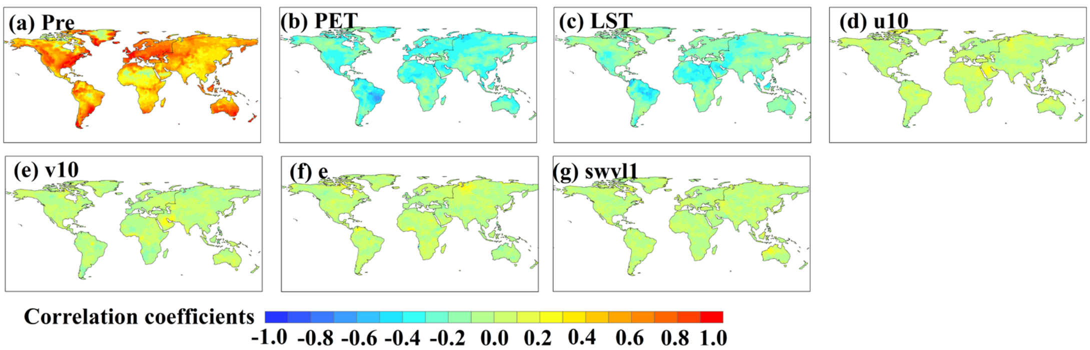

Figure 5. Correlation coefficients of potential variables with the SPEI index. The potential variables include precipitation (Pre), potential evapotranspiration (PET), land surface temperature (LST), 10m U wind component (u10), 10m V wind component (v10), evaporation (e), and volumetric soil water layer 1 (swvl1).

4.2 Spatiotemporal Trend Analysis

As shown in Figure 6, a study was conducted on multi-source data spanning 44 years from 1979 to 2022 to analyze the spatial and temporal trends of precipitation (Pre) (a), potential evapotranspiration (PET) (b), land surface temperature (LST) (c), and the SPEI index (d). It is evident from Figure 6 that the multi-source data exhibited highly uneven spatial trend distributions. Specifically, regions with an annual precipitation (Pre) trend coefficient less than -0.2 mm/year are primarily located in the central and southern parts of South America, including parts of Brazil, Bolivia, Argentina, and smaller regions in southern Africa and western North America, accounting for 5.23%. In contrast, regions with an annual precipitation (Pre) trend coefficient greater than 0.3 mm/year are mainly distributed in the southern United States, tropical rainforest regions of South America and Africa, South Asia, and islands near the equator, accounting for 6.68%. Regions with an increasing trend coefficient for annual potential evapotranspiration (PET) greater than 0.15 mm/year are concentrated in areas such as Brazil and Argentina in South America, southern Australia, Europe, Central Asia, eastern East Asia, and northern and southern Africa, accounting for 27.82%. Meanwhile, regions with a trend coefficient less than -0.05 mm/year primarily include the central and northeastern United States and parts of South Asia, accounting for 3.25%. Areas with an increasing trend coefficient for annual land surface temperature (LST) greater than 0.05°C/year are concentrated in eastern and northern North America, Greenland, eastern and northern Russia, the Middle East, and southern Europe, covering 11.47% of the area, mainly due to Arctic warming. Regions with a trend coefficient less than -0.005°C/year include the central parts of North America and very small parts of South America. These trend results emphasize the significance of climate change in these regions. Through the study of the SPEI index trend in Figure 6(d), regions with a trend coefficient less than -0.01/year are distributed over large areas including northern and southern Africa, the Middle East, Central Asia, central and southern South America (Brazil, Argentina, etc.), as well as smaller regions in western Europe, western Australia, and western North America, indicating a trend towards increased drought due to decreased precipitation and increased evaporation in these regions. The results show that, compared to the past, some regions in Africa, Asia, and South America still exhibit a significant trend towards increasing drought, while precipitation in parts of North and South America shows a significant increasing trend, reducing the drought trend. Overall, the analysis indicates an upward trend.

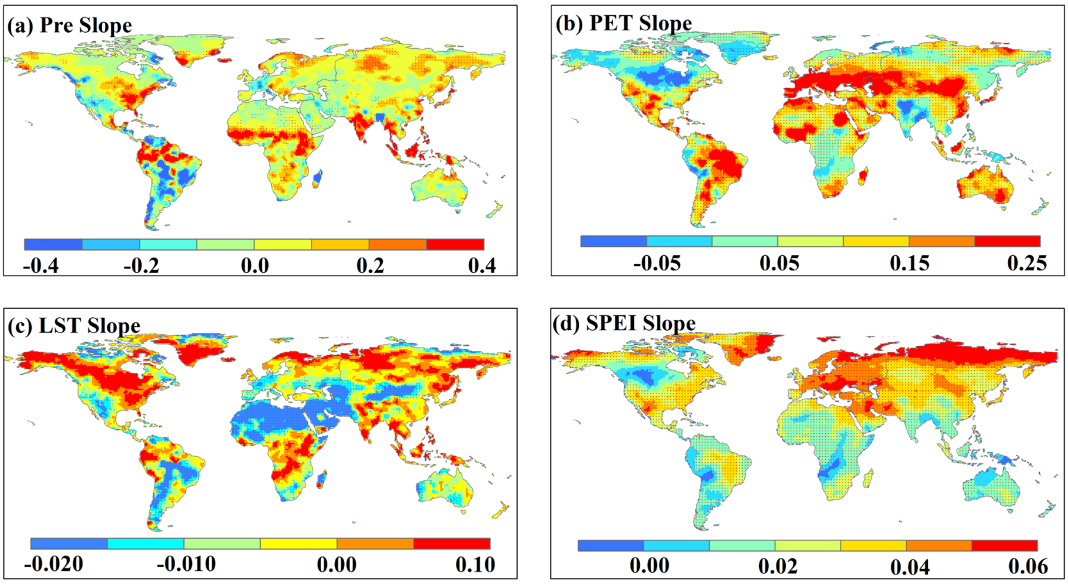

Figure 6. shows the Sen's slope trend analysis for global land from 1979 to 2022: (a) annual precipitation (Pre), (b) annual potential evapotranspiration (PET), (c) annual land surface temperature (LST), and (d) SPEI. The dots indicate trends that passed the 95% confidence level test (red dots indicate an increasing trend, blue dots indicate a decreasing trend; a-b: mm/year; c: °C/year).

We also calculated the average annual trend for each season based on multi-source data. Figure 7 shows significant differences in drought across different seasons and factors. In the spring, the precipitation trend in Figure 7(a) mainly ranges from -0.6 to 0.6 mm/year. Regions in central-southern South America, parts of southern Africa, and southern China (including South China and Southwest China) show a decreasing trend, with the trends being particularly significant in South America and China. The tropical rainforest area of South America and the tropical islands exhibit a significant increasing trend. The potential evapotranspiration trend in Figure 7(e) mainly ranges from -0.1 to 0.4 mm/year, accounting for 91.60% of the area. Areas with a significant increase are located in northern Africa, southern Europe, parts of Central and East Asia, while small parts of North America and South Asia show a significant decreasing trend. Figure 7(i) shows that regions with a significant increase in temperature mainly include most parts of northern Asia. The SPEI trend in Figure 7(m) indicates that areas showing increasing aridity in spring are mainly distributed in northern Africa, South Asia, and northern China. In northern Africa, for example, the increased aridity is mainly due to increased potential evapotranspiration and higher temperatures in some areas. In the summer, Figure 7(b) shows that regions with decreasing precipitation mainly include the grassland climate areas of South America, parts of Africa, northwestern China, and parts of Southeast Asia and South Asia. Areas with increasing precipitation are concentrated in the tropical islands, tropical rainforest areas of Africa, South Asia, and eastern China, with an increasing trend coefficient exceeding 0.6 mm/year. In Figure 7(f), regions with a significant increase in potential evapotranspiration are located in Europe and northern China, accounting for 8.16%, while Ethiopia and South Asia show a significant decreasing trend. Figure 7(j) shows that areas with a significant increase in temperature gradually move southward, including regions in Europe and northern China. Figure 7(n) shows that areas experiencing increasing aridity in summer are mainly located in Brazil, northern Africa, and the Middle East, primarily due to increased potential evapotranspiration. In the autumn, Figure 7(c) shows that precipitation increases in low-latitude areas, while the grassland climate areas of central South America show a decreasing trend in precipitation. Figure 7(g) shows that the trend of increasing potential evapotranspiration is notable in Brazil, parts of northern and southern Africa, while it decreases in South Asia. Figure 7(k) shows a significant increase in temperature trends along the Arctic coastal regions, which are starting to move to higher latitudes. Figure 7(o) shows that drought phenomena will occur in northern and southern Africa and Brazil, closely related to precipitation. In the winter, Figure 7(d) shows that areas with a significant decrease in precipitation are mainly concentrated in Brazil and Argentina. Compared with autumn, the areas with increasing precipitation remain consistent, with the increasing trend areas aligning with the spring precipitation pattern. The regions with significant changes in precipitation exhibit a trend that varies from south to north and back to south with the seasons. Figure 7(h) shows that areas with an increase in potential evapotranspiration are mainly distributed in a few low-latitude regions. Figure 7(l) shows that regions with a significant increase in temperature continue to move north. Figure 7(p) shows that areas experiencing increasing aridity in winter remain consistent with those in autumn. From a global perspective, regions with significant fluctuations in drought trends are mainly concentrated in Africa, Asia, and South America. The frequency density plots indicate that the seasonal trends in precipitation remain consistent, while the density trend of potential evapotranspiration shifts to the right first and then to the left, indicating an initial increase followed by a decrease in potential evapotranspiration. Temperature shows the same trend pattern.

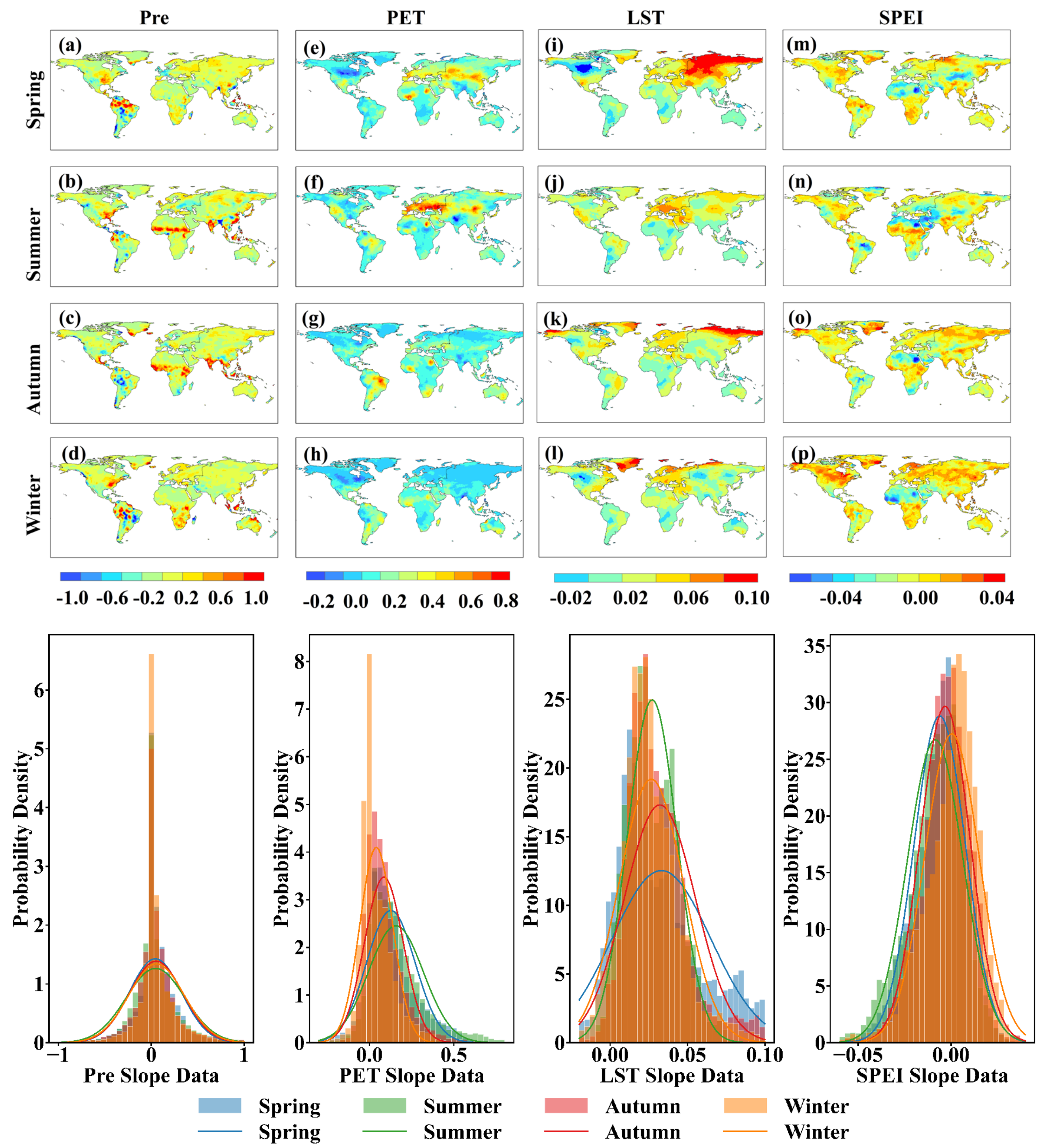

Figure 7 shows the annual trend analysis of the four seasons globally from 1979 to 2022. Specifically, (a, e, i, m) represent spring, (b, f, j, n) represent summer, (c, g, k, o) represent autumn, and (d, h, l, p) represent winter. The figure includes histograms and frequency density curves (a-h: mm/year; i-l: °C/year).

4.3 Drought Characteristics

Figure 8 (a, c, and e) show the annual mean drought duration, severity, and intensity of the SPEI index from 1979 to 2022; Figure 8 (b, d, and f) display the spatial trends of annual mean drought duration, severity, and intensity of the SPEI index from 1979 to 2022. We conducted a comprehensive spatiotemporal analysis of the SPEI index over global land to thoroughly investigate the trends and characteristics of drought events during the period from 1979 to 2022. As shown in Figure 8 (a and b), the duration of droughts worldwide is mostly around 1-2 months, accounting for 62.34%. Droughts lasting more than 2 months are primarily distributed in northern and southern Africa, northern and southern South America, Asia (such as the Middle East, East Asia, etc.), western North America, and Australia, accounting for 11.68%. Trend analysis reveals an increasing trend in drought duration in regions like North Africa, South America (e.g., Brazil, Argentina), Central Asia, and the Middle East. Figure 8c shows that the spatial distribution of drought severity is similar to the spatial distribution of increasing drought duration. Areas with drought severity greater than 3 cover a relatively large area, accounting for 11.20%. Figure 8d shows that the total area where drought severity is decreasing is much larger than the area where severity is increasing. Notably, regions such as Asia and North America show a significant downward trend in drought severity, while areas with increasing severity are mainly concentrated in South America (e.g., Brazil, Argentina), northern and southern Africa, Australia, Central Asia, and the Middle East, accounting for 34.79%. This phenomenon suggests that these regions may experience a substantial short-term cumulative impact of meteorological droughts due to long sunshine duration and high potential evapotranspiration, exacerbating the drought impact. As shown in Figure 8e, 90.45% of the regions have drought intensity in the range of 0.6-0.8, with regions having intensity greater than 0.8 mainly distributed in parts of Asia, Africa, and South America, accounting for 5.19%. Figure 8f shows that the total area where drought intensity is increasing is larger than the area where intensity is decreasing, with regions showing a significant increase in drought intensity distributed in parts of Africa, North America, Asia, and a few areas in South America, accounting for 4.83%.

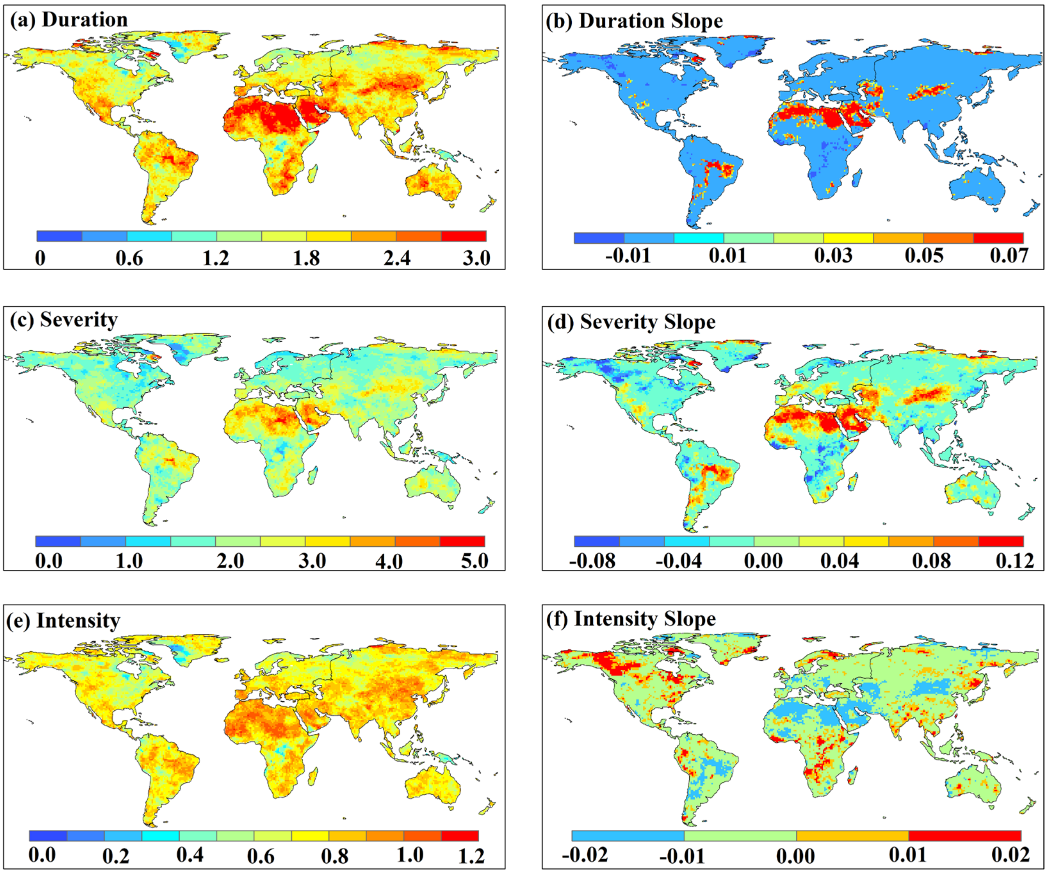

Figure 8 (a, c, e, and g) shows the annual average drought duration, severity, intensity, and frequency based on the SPEI index from 1979 to 2022; (b, d, and f) shows the spatial trends of annual average drought duration, severity, and intensity based on the SPEI index from 1979 to 2022(a: month; b: month/year).

We also calculated the average annual drought duration, severity, and intensity for each season. Since some pixels did not experience drought during a specific season in a given year, the spatiotemporal data is discontinuous, and we did not calculate trends. Figure 9 shows significant differences in drought across seasons. In Figure 9a-d, we observe that in spring, drought duration is longer in certain regions such as northern Africa, Brazil in South America, South Asia, and East Asia. This is consistent with areas with a high frequency of drought occurrence. Globally, the spatial pattern of drought duration is opposite to that of severity, mainly distributed in certain regions of North America, Asia, South America, and Africa. The areas with high severity and intensity are similar, but the areas with high intensity are smaller than those with high severity. In Figure 9e-h, during summer, the drought frequency and severity are higher, and the duration is longer in some parts of northern Africa, due to higher potential evapotranspiration and lower precipitation in this region (Figure 7b-f). At the same time, countries such as China, North Asia, the United States, and Brazil also exhibit high drought intensity, severity, and frequency. Figure 9i-l show that in autumn, areas with longer drought duration and higher frequency are concentrated in northern Africa, southern Africa, Asia, central and southern South America, western Australia, the United States, and Europe. This is due to reduced precipitation. The spatial patterns of severity and intensity are opposite to these, distributed across various regions on different continents. Figure 9m-p indicate that in winter, regions such as Brazil in South America, northern Africa, and Asia have greater drought duration, frequency, and intensity. The high evapotranspiration in these regions may be a contributing factor to the occurrence of drought (Figure 7h). According to the density histogram, spring dominates in terms of duration, indicating that droughts analyzed through run theory last longer in spring. Autumn shows relatively higher severity and intensity, indicating significant events in this season as well. The frequency of drought events is relatively consistent across the four seasons, suggesting that drought is not confined to any specific season and can occur throughout the year.

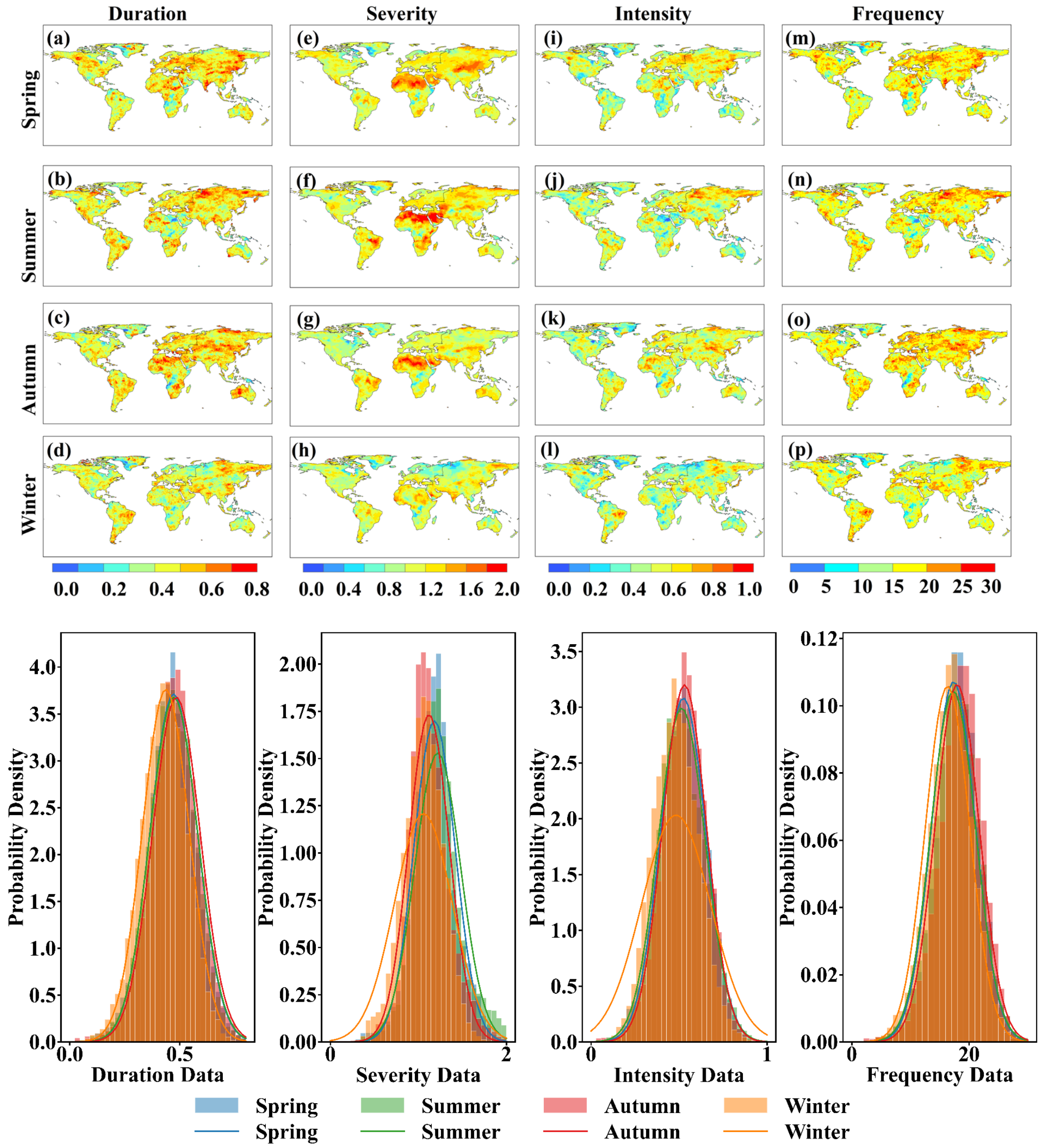

Figure 9. Global drought duration, severity, intensity, and frequency of occurrence for the four seasons from 1979 to 2022. Panels (a, e, i, m) represent spring, (b, f, j, n) represent summer, (c, g, k, o) represent autumn, and (d, h, l, p) represent winter. The figure includes histograms and frequency density curves (a-d: month; m-p: times).

4.4 Overall Performance of Prediction Models

According to Figure 10(a), the evaluation of the two models on the test set shows that the WT-LSTM model has relatively higher prediction accuracy compared to the single LSTM model. In the first scheme, the WT-LSTM model's accuracy is 41% higher than that of the LSTM model, and in the second scheme, it is 30% higher. Therefore, the WT-LSTM model can more effectively capture information from both temporal and spatial dimensions. Furthermore, comparing the accuracy of the WT-LSTM model in the two schemes: the first scheme (MAE=0.035，MSE=0.002，RMSE=0.044，RSR=0.336，RSD=0.993，NSE=0.886，R=0.946) and the second scheme (MAE=0.038，MSE=0.002，RMSE=0.049，RSR=0.371，RSD=0.824，NSE=0.861，R=0.967) (Table 1-2), shows that the WT-LSTM model's prediction accuracy is higher in the second scheme.

We also evaluated the performance for each season. Figure 10(b) show that for each season, the performance of all models is similar to that shown in Figure10(a). Comparing the two models, the WT-LSTM model has higher accuracy, and between the two schemes, the second scheme is relatively more accurate than the first scheme. Compared to the single LSTM model, the WT-LSTM model, utilizing wavelet transform, can extract multi-scale features of the signal, including high-frequency and low-frequency signals. This allows for better capturing of patterns and trends in time series data. Additionally, wavelets can denoise the data, improving the model's ability to recognize the true patterns of the signals. By combining the advantages of both methods, the WT-LSTM model enhances generalization capability and prediction accuracy.

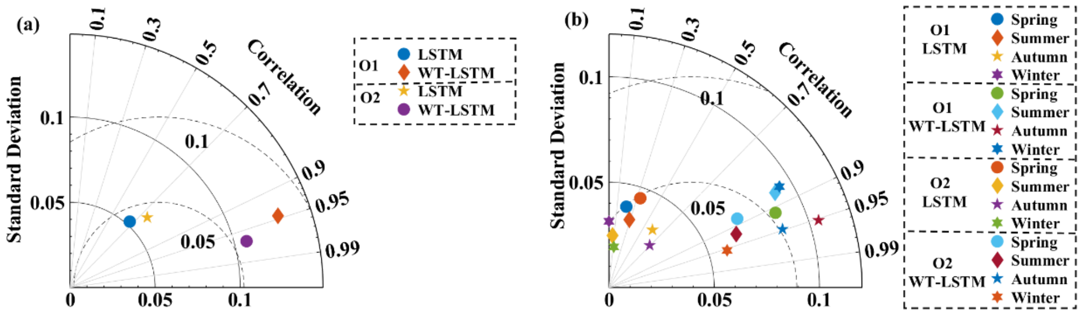

Figure 10 Statistical Comparison of Two Prediction Models (Test Period: 2012-2022; O1 (option): First Option; O2: Second Option) (a) SPEI-1 Values (average of all grid sequences during the test period), (b) SPEI-1 Seasonal Values (average of all grid sequences for each season during the test period: Spring, Summer, Autumn, Winter)

Table 1. Comparison of performance metrics for observed and predicted SPEI in different time periods using the first scheme O1 (Test period: 2012-2022)

Temporal	Model	MAE	MSE	RMSE	RSR	RSD	NSE	R
All data	**LSTM**	0.087	0.011	0.107	0.818	0.402	0.325	0.672
	WT-LSTM	0.035	0.002	0.044	0.336	0.993	0.886	0.946
Spring	**LSTM**	0.082	0.009	0.095	1.170	0.494	-0.416	0.211
	WT-LSTM	0.029	0.002	0.039	0.479	1.090	0.763	0.913
Summer	**LSTM**	0.103	0.016	0.126	1.502	0.408	-1.334	0.287
	WT-LSTM	0.041	0.002	0.049	0.585	1.099	0.646	0.868
Autumn	**LSTM**	0.074	0.008	0.086	0.828	0.334	0.291	0.602
	WT-LSTM	0.027	0.001	0.033	0.314	1.020	0.898	0.952
Winter	**LSTM**	0.081	0.011	0.103	1.108	0.345	-0.269	0.001

	WT-LSTM	0.039	0.002	0.049	0.532	1.033	0.707	0.861

Table2. Comparison of performance metrics for observed and predicted SPEI in different time periods using the first scheme O2 (Test period: 2012-2022)

Temporal	**Model**	**MAE**	**MSE**	**RMSE**	**RSR**	**RSD**	**NSE**	**R**
All data	**LSTM**	0.084	0.010	0.101	0.772	0.471	0.398	0.741
	WT-LSTM	0.038	0.002	0.049	0.371	0.824	0.861	0.967
Spring	**LSTM**	0.074	0.007	0.086	1.058	0.565	-0.158	0.332
	WT-LSTM	0.040	0.002	0.047	0.580	0.869	0.652	0.881
Summer	**LSTM**	0.101	0.014	0.120	1.425	0.300	-1.102	0.070
	WT-LSTM	0.029	0.001	0.037	0.435	0.793	0.804	0.921
Autumn	**LSTM**	0.075	0.008	0.090	0.864	0.272	0.227	0.694
	WT-LSTM	0.033	0.002	0.041	0.390	0.848	0.843	0.948
Winter	**LSTM**	0.074	0.009	0.093	1.000	0.213	-0.034	0.118
	WT-LSTM	0.047	0.004	0.059	0.640	0.646	0.576	0.954

4.5 Ground Validation

In analysis, we selected multiple stations from around the world for the validation of the Standardized Precipitation Evapotranspiration Index (SPEI). Through detailed analysis and screening, we chose several representative stations for in-depth research and analysis. These stations are located in six typical regions: China, Kenya, Italy, Australia, the United States, and Argentina. Figure 11-12 display the correlation graphs for the six typical regions under the two schemes. First, we conducted SPEI predictions using Schemes O1 and O2 for stations in six geographic locations: China (A), Kenya (B), Italy (C), Australia (D), the United States (E), and Argentina (F). In terms of the correlation coefficient (R), Scheme O1 achieved an R of 0.802 for China, 0.841 for Kenya, 0.822 for Italy, 0.798 for Australia, 0.820 for the United States, and 0.812 for Argentina. The results for Scheme O2 were 0.918, 0.921, 0.916, 0.912, 0.916, and 0.920, respectively. This indicates that Scheme O2 significantly outperformed Scheme O1 in terms of R. Secondly, we evaluated the prediction results using the Nash-Sutcliffe Efficiency (NSE) and Mean Absolute Error (MAE). For NSE, Scheme O1 achieved 0.621, 0.686, 0.670, 0.632, 0.661, and 0.653 for China, Kenya, Italy, Australia, the United States, and Argentina, respectively. Scheme O2 achieved 0.833, 0.827, 0.837, 0.821, 0.830, and 0.840, respectively. In terms of MAE, Scheme O1 resulted in 0.482, 0.440, 0.452, 0.485, 0.447, and 0.453, while Scheme O2 resulted in 0.312, 0.328, 0.310, 0.330, 0.306, and 0.299. Overall, Scheme O2 demonstrated better predictive performance in terms of NSE and MAE, making its predictions closer to the actual observations. Scheme O2 combines multiple meteorological factors, allowing for a more comprehensive description of climate change and the hydrological cycle. In contrast, Scheme O1, which predicts the SPEI index sequence alone, fails to capture the complex relationships between different meteorological factors. Integrating multiple meteorological factors into the prediction model enhances the understanding of the dynamic processes of the climate system, captures the impacts of climate change, and better describes the complexity of the climate system. This improvement aids in enhancing the model's explanatory and predictive capabilities regarding drought variability.

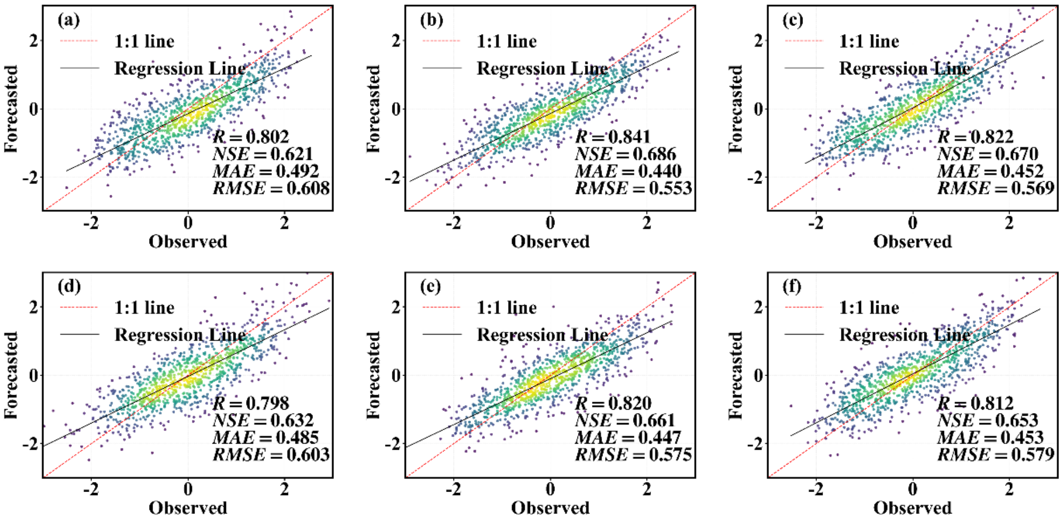

Figure 11. O1 Scheme Typical Regional Station Verification Scatter Plot (O1: First Scheme; Testing Period: 2012-2022; China (A-a), Kenya (B-b), Italy (C-c), Australia (D-d), USA (E-e), Argentina (F-f))

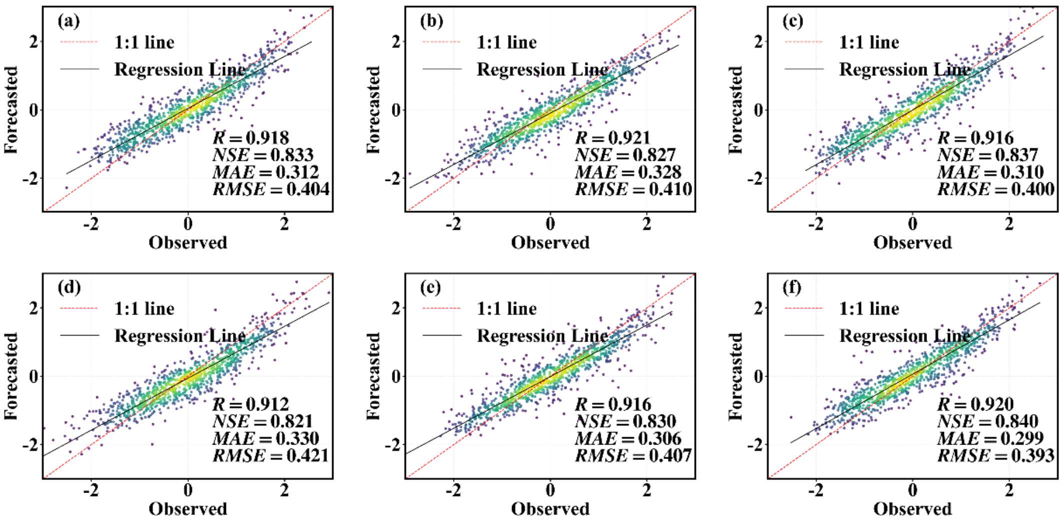

Figure 12. Scatter Plot of O2 Scheme for Typical Regional Stations (O2: Second Scheme; Test Period: 2012-2022; China (A-a), Kenya (B-b), Italy (C-c), Australia (D-d), USA (E-e), Argentina (F-f))

4.6 Cross-Validation

Cross-validation is crucial for identifying spatial differences between products and prediction results. It requires considering the spatial resolution of different datasets, data generation methods, and changes over time. Specifically, by selecting test period intervals, we can group the data within the study area by four seasons and calculate the average value for each season to perform cross-validation. This approach allows us to study the differences between prediction results and products from multiple temporal scales, providing a more comprehensive data basis for comprehensive evaluation (a-c spring; d-f summer; g-i autumn; j-l winter; histograms represent the frequency of differences), as shown in Figure 13. The comparison between the SPEIBase product and the prediction results of the two schemes shows relatively consistent spatial distribution, with differences observed in some areas. The correlation coefficients R for the first scheme's validation results across the four seasons are 0.778, 0.818, 0.755, and 0.762, with MAE errors of 0.090, 0.087, 0.091, and 0.070, respectively. For the second scheme, the correlation coefficients R are 0.853, 0.874, 0.837, and 0.815, with MAE errors of 0.069, 0.070, 0.070, and 0.094, respectively. Comparatively, the second scheme has higher prediction accuracy. Spatially, the four seasons primarily show differences in drought-prone areas in northern and southern Africa, South America, and parts of Asia, leading to changes in drought levels. The difference frequency histograms for the four seasons show that the prediction result differences follow a normal distribution, indicating good error stability and small variability between data points.

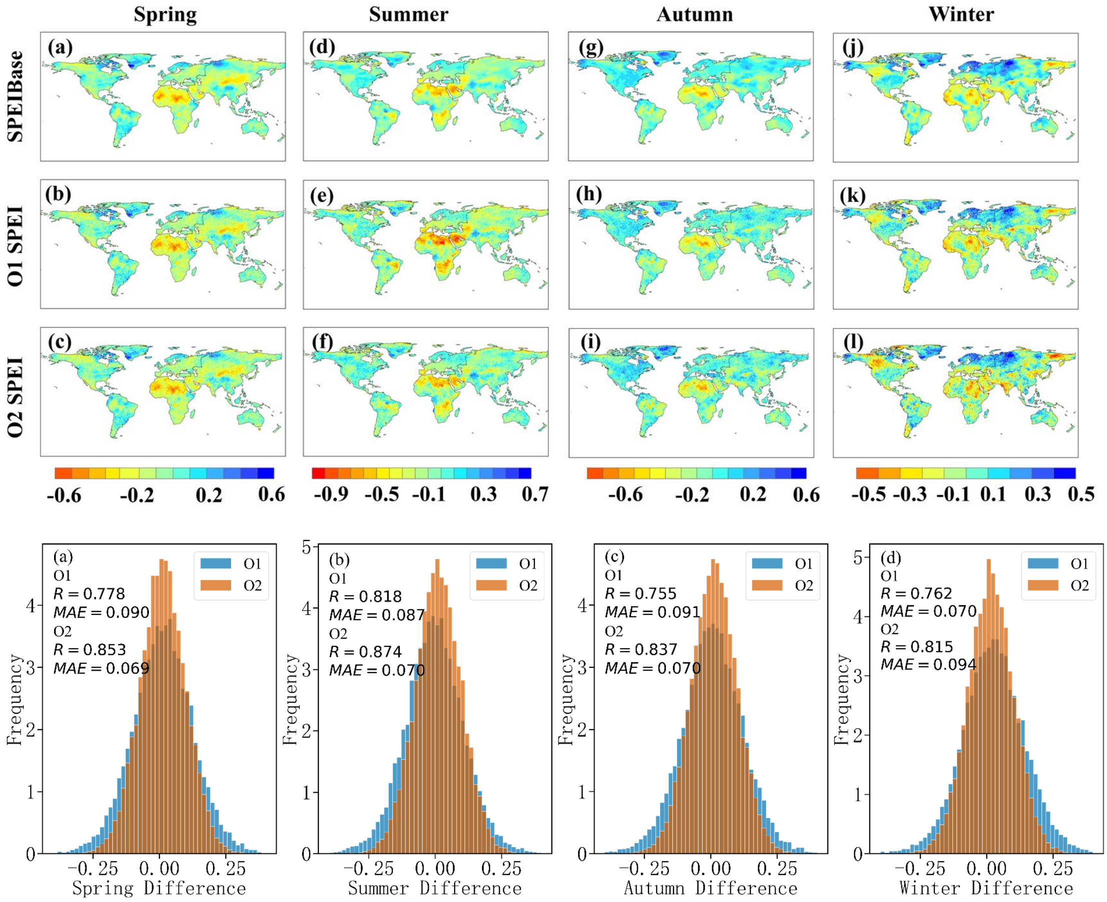

Figure 13. Comparison of model prediction results of two schemes with existing product results (test period: 2012-2022) (a-c spring; d-f summer; g-i autumn; j-l winter); Histograms represent the difference frequency (O1 indicates the difference of the first scheme, O2 indicates the difference of the second scheme, and the error accuracy of both schemes is marked).

4.7 Identification and Reconstruction Analysis of Drought Characteristics in Typical Drought-Prone Regions by the Prediction Model

Based on the spatiotemporal analysis in Sections 4.2 and 4.3, the study shows that drought-prone areas are mainly distributed across Africa, South America, Asia, and other regions. To evaluate the model's ability to identify and reconstruct drought characteristics, this study selects typical drought-prone regions including North Africa, South America, North America, Asia, and Australia (as shown in Figure 14). A hybrid model combining wavelet transform (WT) and long short-term memory neural network (LSTM), referred to as WT-LSTM, is employed to simulate drought characteristics from 2013 to 2022.By comparing two schemes (O1 and O2), the prediction error distributions of annual average drought duration, intensity, severity, and frequency are analyzed, as shown in Tables 3, Tables 4 , Figure 4-15.

The results indicate that Scheme O2 significantly outperforms O1 in prediction accuracy across all regions. In terms of the frequency of drought duration deviations within the range [-1, 1], Africa improved from 72.48% (O1) to 93.50% (O2), Asia from 85.41% to 96.84%, and North America reached 99.07%. For drought intensity, prediction accuracy in Africa increased by 12.17%, and in Australia by 22.75%. Although drought severity remains more challenging to predict, O2 still achieved slight improvements in most regions. Notably, O2 excelled in zero-error prediction capability; for instance, the frequency of exact matches in drought intensity (error = 0) in Africa rose from 35.34% to 59.90%. North America showed the best overall performance, while South America and Australia also improved compared to O1, albeit to a lesser extent.

Overall, the WT-LSTM model demonstrates strong adaptability and statistical robustness in global drought-prone regions, making it well-suited for drought characteristic identification and prediction. Future improvements may include incorporating high-resolution climate data, attention mechanisms, and climate drivers such as ENSO to further enhance model performance and physical interpretability.

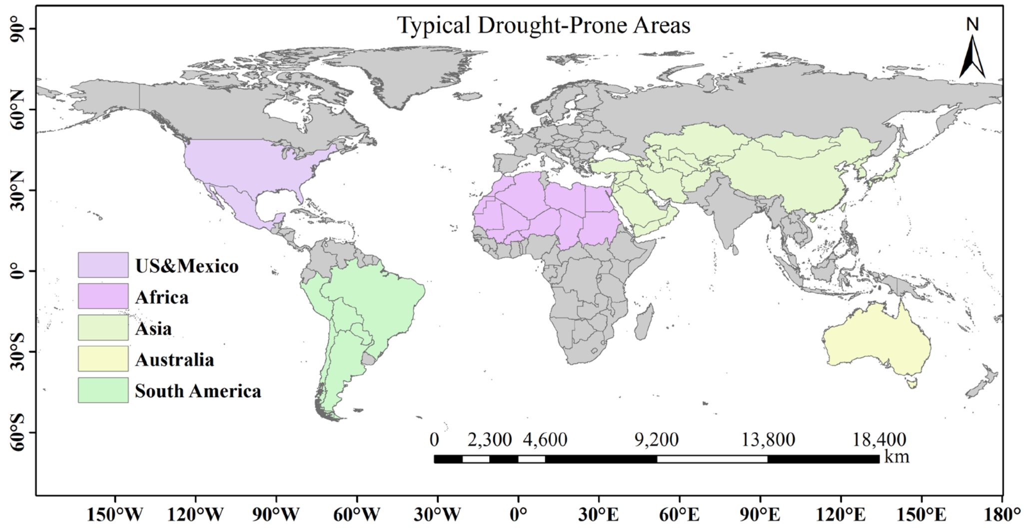

Figure 14. Visualization of Vector Map for Typical Drought-Prone Regions

Table 3. Frequency of Annual Average Drought Characteristic Deviations in Key Regions under Scheme O1 (Test Period: 2013–2022)

Range	Duration		Severity	Intensity	Frequency	
	[-1,1]	0	[-1,1]	[0,5]	[-1,1]	0
Africa	72.48%	4.05%	57.49%	75.97%	79.55%	35.34%
Asia	85.41%	5.02%	69.47%	87.41%	72.07%	31.64%
Australia	76.01%	4.41%	70.02%	99.12%	63.14%	25.57%
South America	75.55%	5.45%	62.62%	91.56%	64.91%	24.71%
US & Mexico	92.82%	8.10%	89.81%	100%	64.35%	24.65%

Note: Duration is measured in months; frequency is measured in occurrences; severity and intensity are dimensionless.

Table 5. Frequency of Annual Average Drought Characteristic Deviations in Key Regions under Scheme O2 (Test Period: 2013–2022)

Range	Duration		Severity	Intensity	Frequency	
	[-1,1]	0	[-1,1]	[0,5]	[-1,1]	0
Africa	93.50%	9.99%	64.09%	74.36%	91.72%	59.90%
Asia	96.84%	13.10%	75.56%	85.69%	89.82%	56.04%
Australia	96.12%	14.64%	82.72%	99.12%	85.89%	44.80%
South America	96.57%	14.16%	76.96%	90.59%	84.96%	47.76%
US & Mexico	99.07%	16.32%	95.02%	99.65%	82.18%	40.28%

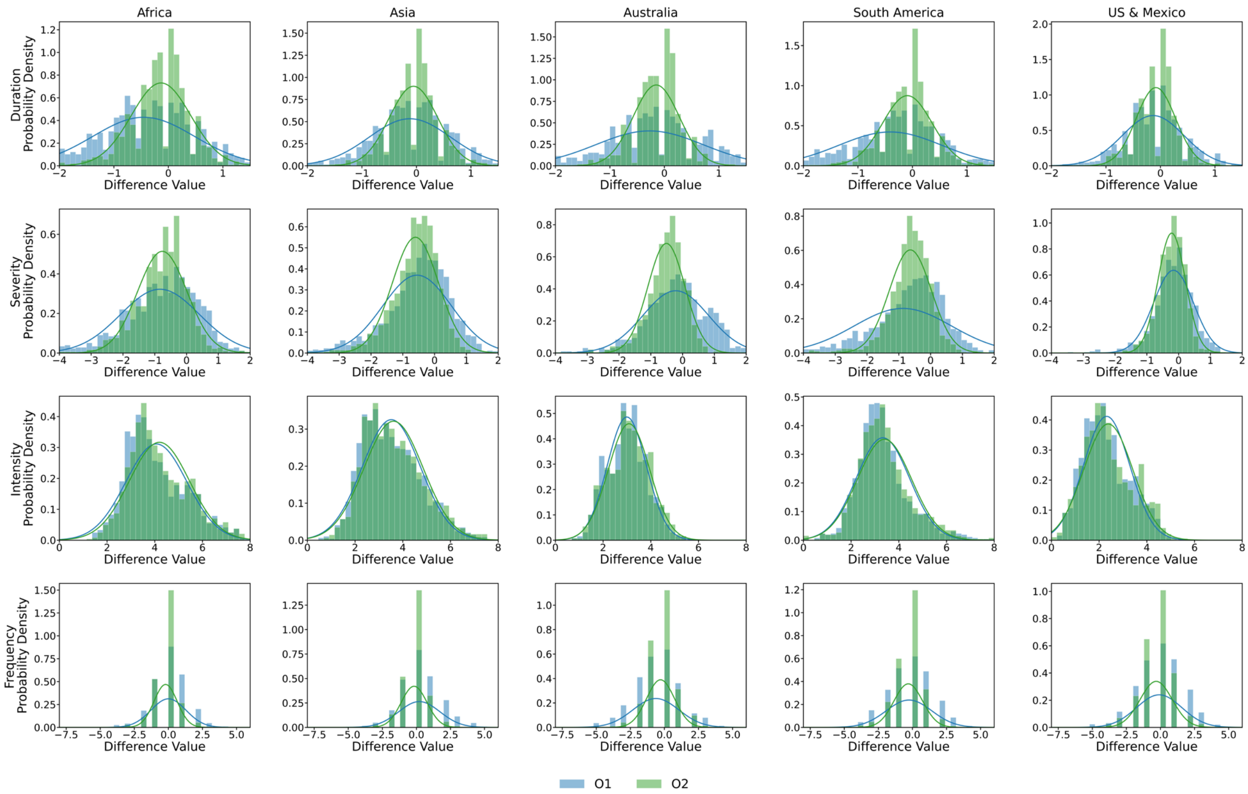

Figure 4-15. Histograms and Probability Densities of Drought Characteristic Deviations in Key Regions under Two Schemes (O1 and O2) (Test Period: 2013–2022)

4.9 Trend Analysis of Predicted Drought Conditions in Typical Drought-Prone Regions for 2023–2024

This study combines wavelet decomposition and LSTM models to evaluate the accuracy of drought trend predictions over the next 10 years (2013–2022), with a final focus on the upcoming 24 months (2023–2024). This emphasis on short-term prediction is due to the decreasing accuracy of long-term forecasts; beyond 6–7 years, model reliability declines significantly. In contrast, short-term predictions (e.g., two years) better capture drought dynamics and offer more practical value. By decomposing the precipitation time series into multi-scale components—low-frequency (A3) and high-frequency (D1–D3)—and modeling them separately, the prediction performance of LSTM is notably enhanced across different frequency bands. Results show high prediction accuracy for low-frequency components, with strong short-term correlation between SPEI and meteorological variables ($R = 0.91$ for 1-year), but a drop to 0.03 over 10 years, confirming the greater reliability of short-term forecasts (see Tables 6 and 7). Figure 4-16 illustrates projected drought trends in five typical drought-prone regions during 2023–2024. Historically, North Africa exhibits the most severe drought intensification (slope = -0.001715), and although the trend slightly slows in 2023–2024, it remains the steepest. Asia and South America show similar, sustained trends (around -0.00084); Australia's drought trend shows notable weakening (slope = -0.000134 in Scheme 1), possibly due to changes in precipitation patterns; while the U.S.–Mexico region exhibits the weakest and most stable trend (-0.000099). Overall, global drought-prone areas continue to experience intensifying drought, with North Africa being the most prominent and Australia showing signs of potential relief.

Table 6. Evaluation of Predicted vs. Observed Global Land SPEI Values under Scheme 1 (O1) for 2013–2022 (Correlation Coefficient R)

	1 年	2 年	3 年	4 年	5 年	6 年	7 年	8 年	9 年	10 年
A3	0.91	0.58	0.46	0.29	0.13	0.23	0.22	0.13	0.02	0.04
D1	-0.33	-0.32	-0.23	-0.21	-0.20	-0.18	-0.17	-0.17	-0.17	-0.17
D2	0.51	0.13	0.24	0.22	0.16	0.14	0.09	0.06	0.06	0.06
D3	0.58	0.30	0.29	0.23	0.21	0.13	0.05	0.04	-0.00	-0.02
SPEI	0.88	0.53	0.38	0.29	0.25	0.20	0.13	0.10	0.06	0.05

Note: The vertical axis represents variables — A3 denotes the low-frequency component, while D1, D2, and D3 represent high-frequency components. The horizontal axis represents years.

Table 7. Evaluation of Global Land Predicted vs. Observed Values (Correlation Coefficient R) under Scheme 2 (O2), 2013–2022

	1 年	2 年	3 年	4 年	5 年	6 年	7 年	8 年	9 年	10 年
SPEI	0.91	0.52	0.29	0.15	0.09	0.10	0.09	0.06	0.04	0.03

Note: The vertical axis represents the SPEI variable, and the horizontal axis represents the year.

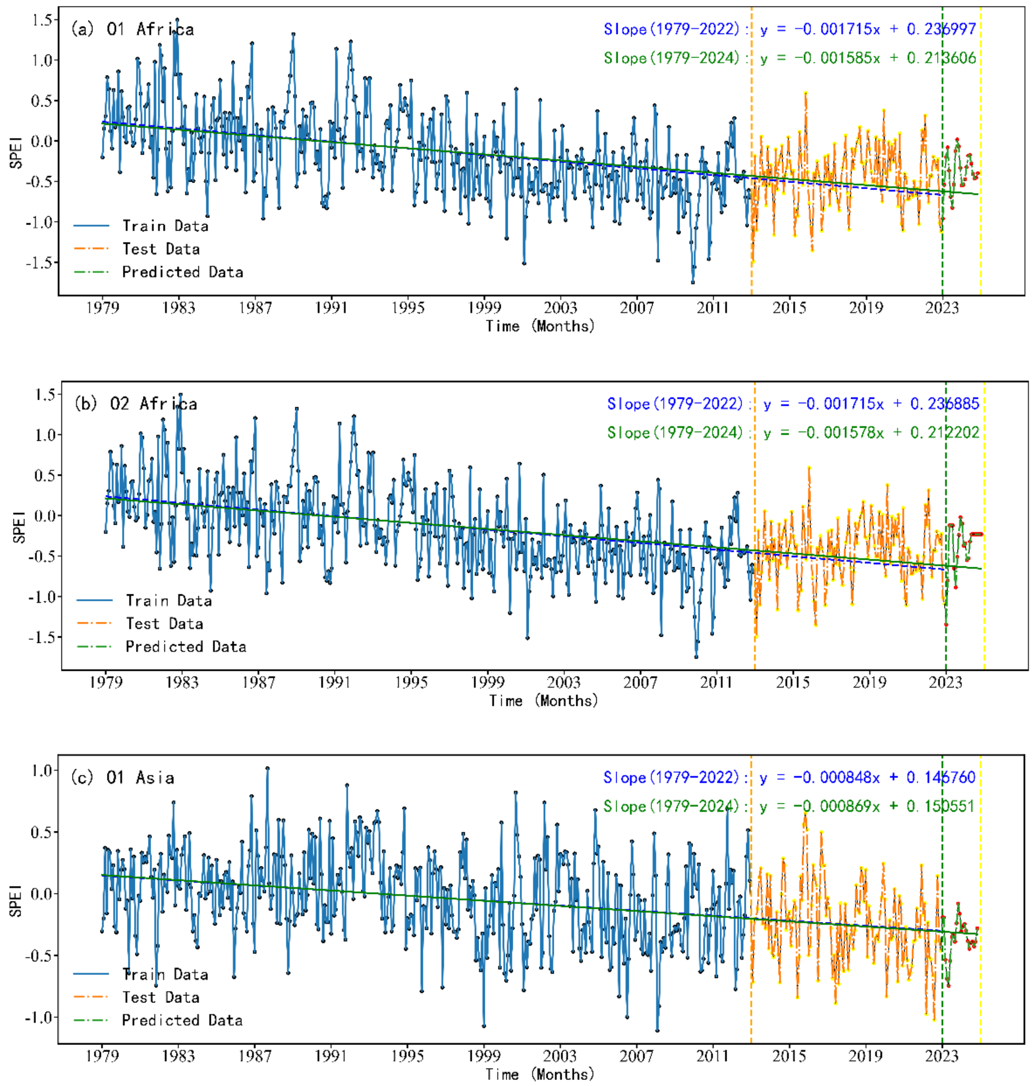

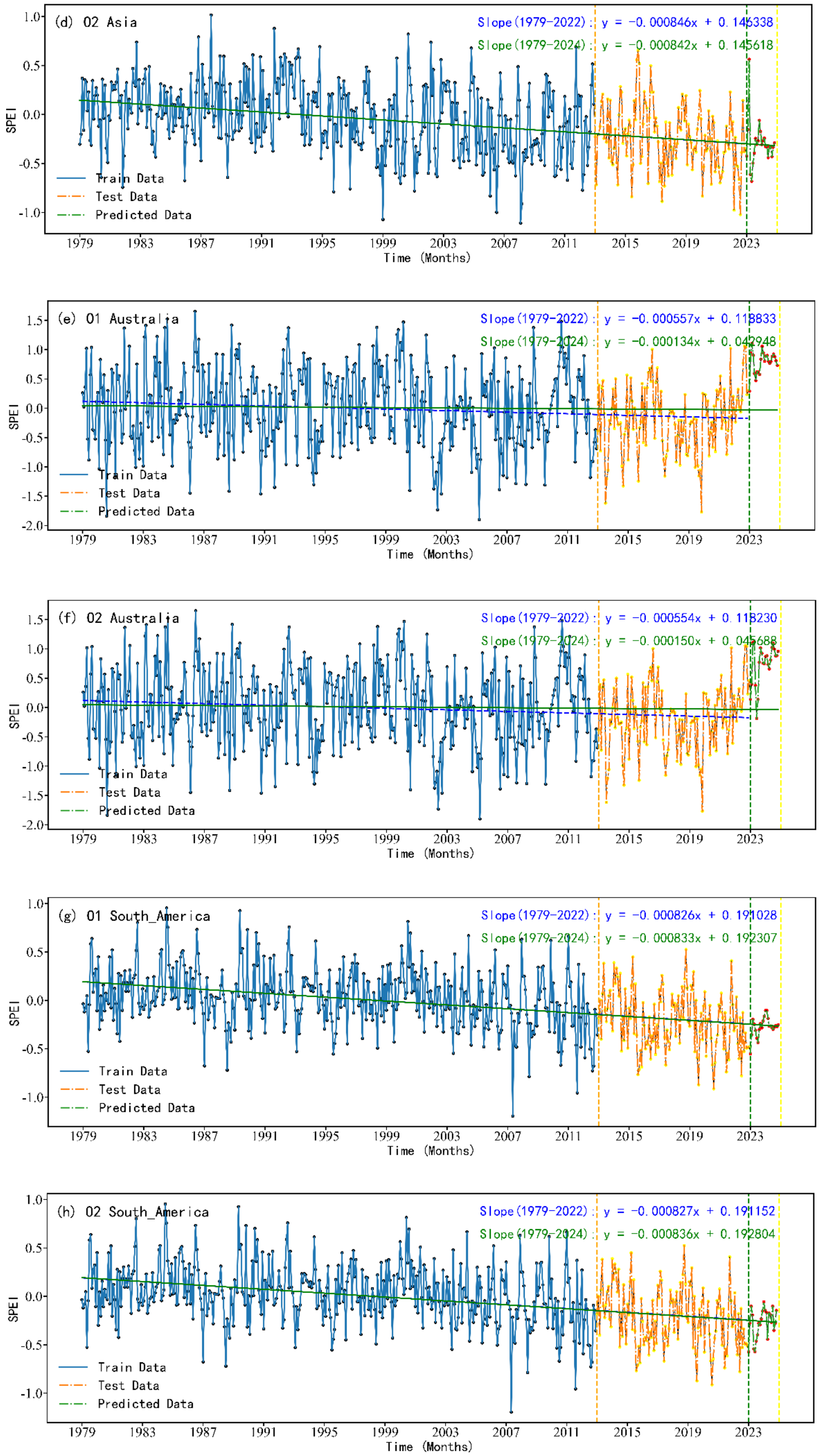
(d) 02 Asia
Slope(1979-2022): y = -0.000846x + 0.145338
Slope(1979-2024): y = -0.000842x + 0.145618
Train Data
Test Data
Predicted Data
SPEI
Time (Months)
(e) 01 Australia
Slope(1979-2022): y = -0.000557x + 0.118833
Slope(1979-2024): y = -0.000134x + 0.042948
Train Data
Test Data
Predicted Data
SPEI
Time (Months)
(f) 02 Australia
Slope(1979-2022): y = -0.000554x + 0.118230
Slope(1979-2024): y = -0.000150x + 0.045688
Train Data
Test Data
Predicted Data
SPEI
Time (Months)
(g) 01 South_America
Slope(1979-2022): y = -0.000826x + 0.191028
Slope(1979-2024): y = -0.000833x + 0.192307
Train Data
Test Data
Predicted Data
SPEI
Time (Months)
(h) 02 South_America
Slope(1979-2022): y = -0.000827x + 0.191152
Slope(1979-2024): y = -0.000836x + 0.192804
Train Data
Test Data
Predicted Data
SPEI
Time (Months)

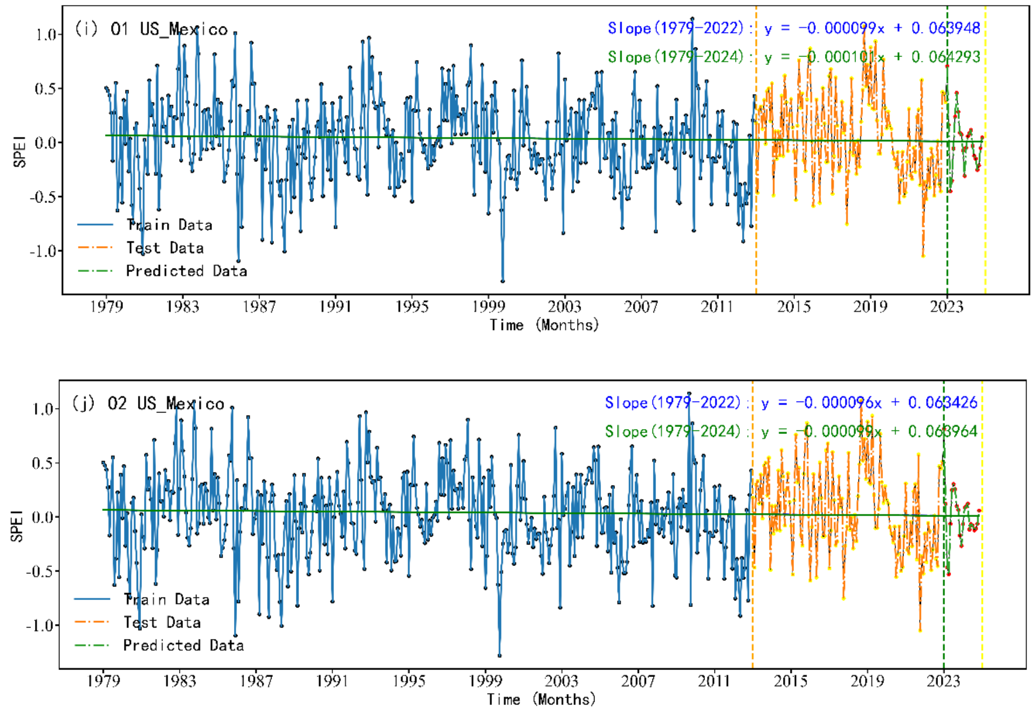

Figure 4-16 Trend Visualization for 2023–2024 under Two Schemes in Five Typical Drought-Prone Regions (Vertical Axis: Dimensionless, Horizontal Axis: Month)

4.10 Drought policy implications

For regions that experience frequent and intense droughts, it is recommended to actively prepare for drought mitigation through the following measures: (1) Adopt Water-Saving Irrigation Techniques: Implement efficient water-saving irrigation methods, such as drip and sprinkler systems, to improve agricultural water use efficiency and reduce water wastage. (2) Water Resource Reuse: Promote water reuse technologies, such as rainwater harvesting and wastewater treatment, to provide additional water supply. (3) Improve Soil Moisture Management: Enhance soil management practices, such as conservation tillage, to reduce soil moisture evaporation losses and improve soil water retention capacity. (4) Construct Reservoirs and Waterworks: Build reservoirs and water infrastructure in drought-prone areas to increase water resource storage and supply capacity, thereby alleviating drought impacts. (5) Establish Water Resource Management Mechanisms: Develop robust water resource management systems, including resource allocation and usage management, to ensure sustainable utilization of resources. (6) Implement Water Resource Monitoring and Early Warning Systems: Establish strengthened monitoring and early warning systems for water resources and drought to provide real-time assessments of water status and advance warnings for droughts. (7) Enhance Agricultural Production Efficiency: Improve agricultural production efficiency by selecting appropriate farming methods, crop structures, and irrigation techniques, thereby reducing dependence on water resources.

Additionally, for areas that have long been affected by drought, consider the following strategies: (1) Regional Water Use Restrictions: Implement regional water use policies to limit consumption and reduce wastage, ensuring sustainable resource use. (2) Water Resource Allocation: Optimize the distribution of water resources by transferring supplies from water-rich areas to water-scarce regions to alleviate drought issues and ensure water availability. (3) Strengthen Drought Monitoring and Early Warning: Enhance drought monitoring and early warning efforts to provide timely information and guidance to residents and farmers, enabling effective measures to minimize drought-related losses.

In the context of global sustainable development challenges such as climate change and resource depletion, implementing these measures is particularly important. Future research should focus on exploring innovative water resource management and water-saving technologies, promoting interdisciplinary collaboration to more effectively address drought issues and provide scientific evidence for global sustainable development. Through such efforts, we can better tackle the challenges posed by drought and lay the groundwork for a sustainable future.

5. Conclusion

Meteorological drought is the precursor to hydrological and agricultural droughts. Monitoring and forecasting short-term meteorological droughts can effectively mitigate the damages and impacts caused by droughts. By analyzing precipitation (Pre), potential evapotranspiration (PET), land surface temperature (LST), and the Standardized Precipitation-Evapotranspiration Index (SPEI), we can examine the spatiotemporal distribution characteristics of meteorological drought on a monthly scale. Additionally, we compare the predictions of global land data using a hybrid model (WT-LSTM) across two different schemes to validate the applicability of the hybrid model in drought prediction and to highlight the differences and similarities between the two prediction methods.

From 1979 to 2022, due to factors such as reduced precipitation and increased potential evapotranspiration, regions in Africa, South America, and Asia have shown a significant trend towards increased drought, while parts of North America and South America have exhibited a significant increase in precipitation. Overall, the trend analysis indicates a slow upward trend in general. The spatiotemporal distribution of meteorological drought varies significantly across different seasons. During the summer and autumn, the duration, frequency, and intensity of droughts are highest in northern Africa. In contrast, during the spring and winter, regions such as Brazil in South America, North Africa, and South Asia experience long-duration, high-frequency, and intense droughts.

Among the two schemes, the first scheme demonstrated the best test performance, with the second scheme achieving R values above 0.9. The WT-LSTM hybrid model effectively addresses the issue of non-stationarity in short-term meteorological time series, demonstrating its applicability. The comparison between the two schemes revealed a high degree of spatial consistency. Both schemes show significant advantages in drought prediction, each excelling in predicting different types of drought conditions.

To address the complex interdisciplinary issue of meteorological drought, it is essential to emphasize its relevance to global sustainable development challenges. Future research should further explore the roles of additional meteorological and environmental variables in drought prediction, integrating advanced data analysis techniques to continually optimize prediction methods. Interdisciplinary collaboration and research will be crucial in tackling these challenges, raising awareness among policymakers and the public regarding drought issues, and providing a scientific basis for formulating more effective response strategies. By enhancing cooperation across various fields, we can develop more comprehensive and effective strategies to support the achievement of global sustainable development goals.

Author contributions

JB and KM designed the research and developed the methodology. JB, KM and XX contributed to the analysis and discussion of the results. JB drafted the manuscript, and all the authors(JB, KM, XX, JS, BMS, YZ) revised the manuscript.

Declaration of Competing Interest

The authors declare that they have no known competing financial interests or personal relationships that could have appeared to influence the work reported in this paper.

Data availability

The data that support the findings of this study are openly available in the Open Science Framework data repository, including data from the European Centre for Medium-Range Weather Forecasts (ECMWF) for providing precipitation and other meteorological data (https://cds.climate.copernicus.eu/datasets), the Climatic Research Unit for supplying the SPEIbase dataset and related reanalysis meteorological data (https://spei.csic.es/database.html), and the National Oceanic and Atmospheric Administration (NOAA) for providing station-based observation data (https://www.ncei.noaa.gov/maps/monthly/).

Acknowledgments

The authors are grateful to three reviewers and the editor for their constructive comments and suggestions on this paper. The authors extend their heartfelt appreciation to ECMWF for providing the climate reanalysis product and TensorFlow for offering the sophisticated machine learning library that served as the cornerstone for conducting these experiments. This research was supported by Central Public-interest Scientific Institution Basal Research Fund (No. Y2025YC86) and the Key Project of Natural Science Foundation of Ningxia Department of Science and Technology (No. 2024AC02032), for which we are deeply grateful.

References

Asgarimehr, M., C. Arnold, T. Weigel, et al. (2022) GNSS reflectometry global ocean wind speed using deep learning: Development and assessment of CyGNSSnet. *Remote Sensing of Environment,* 269**,** 112801.

Cailas, M. D., G. Cavadias & R. Gehr (1986) Application of a Nonparametric Approach for Monitoring and Detecting Trends in Water Quality Data for the St. *Water Quality Research Journal,* 21**,** 153-167.

Chiew, F. & T. McMahon (1993) Detection of trend or change in annual flow of Australian rivers. *International Journal of Climatology,* 13**,** 643-653.

Cui, G., Q. Ma & R. Bales (2022) Assessing multi-year-drought vulnerability in dense Mediterranean-climate forests using water-balance-based indicators. *Journal of Hydrology,* 606**,** 127431.

Dikshit, A., B. Pradhan & A. M. Alamri (2021) Long lead time drought forecasting using lagged climate variables and a stacked long short-term memory model. *Science of The Total Environment,* 755**,** 142638.

Douglas, E., R. Vogel & C. Kroll (2000) Trends in floods and low flows in the United States: impact of spatial correlation. *Journal of hydrology,* 240**,** 90-105.

Gan, T. Y. (1998) Hydroclimatic trends and possible climatic warming in the Canadian Prairies. *Water resources research,* 34**,** 3009-3015.

Gislason, P. O., J. A. Benediktsson & J. R. Sveinsson (2006) Random forests for land cover classification. *Pattern recognition letters,* 27**,** 294-300.

Guttman, N. B. (1999) Accepting the standardized precipitation index: a calculation algorithm 1. *JAWRA Journal of the American Water Resources Association,* 35**,** 311-322.

Ham, Y.-G., J.-H. Kim & J.-J. Luo (2019) Deep learning for multi-year ENSO forecasts. *Nature,* 573**,** 568-572.

Hao, Z., F. Hao, V. P. Singh, et al. (2016) A theoretical drought classification method for the multivariate drought index based on distribution properties of standardized drought indices. *Advances in water resources,* 92**,** 240-247.

Hipel, K. W., A. J. McLeod & R. R. Weller (1988) DATA ANALYSIS OF WATER QUALITY TIME SERIES IN LAKE ERIE 1. *JAWRA Journal of the American Water Resources Association,* 24**,** 533-544.

Kim, S., C.-Y. Choi, M. Shahandashti, et al. (2022) Improving accuracy in predicting city-level construction cost indices by combining linear ARIMA and nonlinear ANNs. *Journal of Management in Engineering,* 38**,** 04021093.

Kisi, O. (2011) Wavelet regression model as an alternative to neural networks for river stage forecasting. *Water resources management,* 25**,** 579-600.

Łabędzki, L. (2007) Estimation of local drought frequency in central Poland using the standardized precipitation index SPI. *Irrigation and Drainage: The journal of the International Commission on Irrigation and Drainage,* 56**,** 67-77.

Le, J., H. El-Askary, M. Allali, et al. (2017) Application of recurrent neural networks for drought projections in

California. *Atmospheric research,* 188**,** 100-106.

Lins, H. F. & J. R. Slack (1999) Streamflow trends in the United States. *Geophysical research letters,* 26**,** 227-230.

Liu, J., X. Yuan, J. Zeng, et al. (2022) Ensemble streamflow forecasting over a cascade reservoir catchment with integrated hydrometeorological modeling and machine learning. *Hydrology and earth system sciences,* 26**,** 265-278.

Madhu, S., T. L. Kumar, H. Barbosa, et al. (2015) Trend analysis of evapotranspiration and its response to droughts over India. *Theoretical and applied climatology,* 121**,** 41-51.

Mallat, S. G. (1989) A theory for multiresolution signal decomposition: the wavelet representation. *IEEE transactions on pattern analysis and machine intelligence,* 11**,** 674-693.

Mann, H. B. (1945) Nonparametric tests against trend. *Econometrica: Journal of the econometric society***,** 245-259.

Onoz, B. & M. Bayazit (2003) The power of statistical tests for trend detection. *Turkish Journal of Engineering & Environmental Sciences,* 27.

Peng, J., S. Chen, H. Lü, et al. (2016) Spatiotemporal patterns of remotely sensed PM2. 5 concentration in China from 1999 to 2011. *Remote sensing of environment,* 174**,** 109-121.

Reichstein, M., G. Camps-Valls, B. Stevens, et al. (2019) Deep learning and process understanding for data-driven Earth system science. *Nature,* 566**,** 195-204.

Retsch, M., C. Jakob & M. Singh (2022) Identifying relations between deep convection and the large-scale atmosphere using explainable artificial intelligence. *Journal of Geophysical Research: Atmospheres,* 127**,** e2021JD035388.

Sen, P. K. (1968) Estimates of the regression coefficient based on Kendall's tau. *Journal of the American statistical association,* 63**,** 1379-1389.

Stagge, J. H., L. M. Tallaksen, L. Gudmundsson, et al. (2015) Candidate distributions for climatological drought indices (SPI and SPEI). *International Journal of Climatology,* 35**,** 4027-4040.

Sun, L., S. W. Mitchell & A. Davidson (2012) Multiple drought indices for agricultural drought risk assessment on the Canadian prairies. *International Journal of Climatology,* 32**,** 1628.

Theil, H. (1950) A rank-invariant method of linear and polynomial regression analysis. *Indagationes mathematicae,* 12**,** 173.

Tirivarombo, S., D. Osupile & P. Eliasson (2018) Drought monitoring and analysis: standardised precipitation evapotranspiration index (SPEI) and standardised precipitation index (SPI). *Physics and Chemistry of the Earth, Parts A/B/C,* 106**,** 1-10.

Topaloğlu, F., A. Irvem & M. Özfidaner (2012) Re-evaluation of trends in annual streamflows of Turkish rivers for the period 1968-2007. *Fresenius Environmental Bulletin,* 21**,** 2043-2050.

Trnka, M., M. Dubrovský, M. D. Svoboda, et al. (2008) Developing a regional drought climatology for the Czech Republic.

Vicente-Serrano, S. M., S. Beguería & J. I. López-Moreno (2010) A multiscalar drought index sensitive to global warming: the standardized precipitation evapotranspiration index. *Journal of climate,* 23**,** 1696-1718.

Wang, Q., J. Zeng, J. Qi, et al. (2021) A multi-scale daily SPEI dataset for drought characterization at observation stations over mainland China from 1961 to 2018. *Earth System Science Data,* 13**,** 331-341.

Wang, X. (2022) Research on the prediction of per capita coal consumption based on the ARIMA–BP combined model. *Energy Reports,* 8**,** 285-294.

Wu, J. & X. Chen (2019) Spatiotemporal trends of dryness/wetness duration and severity: The respective contribution of precipitation and temperature. *Atmospheric Research,* 216**,** 176-185.

Xu, D., Q. Zhang, Y. Ding, et al. (2020) Application of a hybrid ARIMA–SVR model based on the SPI for the forecast of drought—a case study in Henan Province, China. *Journal of applied meteorology and climatology,* 59**,** 1239-1259.

Xu, D., Q. Zhang, Y. Ding, et al. (2022) Application of a hybrid ARIMA-LSTM model based on the SPEI for drought forecasting. *Environmental Science and Pollution Research,* 29**,** 4128-4144.

Yang, S., D. Yang, J. Chen, et al. (2019) Real-time reservoir operation using recurrent neural networks and inflow forecast from a distributed hydrological model. *Journal of Hydrology,* 579**,** 124229.

Yevjevich, V. M. 1967. *An objective approach to definitions and investigations of continental hydrologic droughts*. Colorado State University Fort Collins, CO, USA.

Yu, Y.-S., S. Zou & D. Whittemore (1993) Non-parametric trend analysis of water quality data of rivers in Kansas. *Journal of Hydrology,* 150**,** 61-80.

Yue, S. & P. Pilon (2004) A comparison of the power of the t test, Mann-Kendall and bootstrap tests for trend detection/Une comparaison de la puissance des tests t de Student, de Mann-Kendall et du bootstrap pour la détection de tendance. *Hydrological Sciences Journal,* 49**,** 21-37.

Yue, S., P. Pilon & G. Cavadias (2002) Power of the Mann–Kendall and Spearman's rho tests for detecting monotonic trends in hydrological series. *Journal of hydrology,* 259**,** 254-271.

Zetterqvist, L. (1991) Statistical estimation and interpretation of trends in water quality time series. *Water Resources Research,* 27**,** 1637-1648.

Zhang, J. J., L. Sun, D. Rainham, et al. (2022) Predicting intraurban airborne PM1. 0-trace elements in a port city: Land use regression by ordinary least squares and a machine learning algorithm. *Science of the Total Environment,* 806**,** 150149.

Zheng, H., C. Miao, X. Li, et al. (2022) Effects of vegetation changes and multiple environmental factors on evapotranspiration across China over the past 34 years. *Earth's Future,* 10**,** e2021EF002564.